### **Biofabrication**



### **OPEN ACCESS**

### RECEIVED

3 October 2024

### REVISED

28 February 2025

ACCEPTED FOR PUBLICATION 21 March 2025

#### PUBLISHED

1 April 2025

Original content from this work may be used under the terms of the Creative Commons Attribution 4.0 licence

Any further distribution of this work must maintain attribution to the author(s) and the title of the work, journal citation and DOI.



### **PAPER**

# A hollow fiber membrane-based liver organoid-on-a-chip model for examining drug metabolism and transport

Adam Myszczyszyn<sup>1,\*</sup>, Anna Muench<sup>1</sup>, Vivian Lehmann<sup>1</sup>, Theo Sinnige<sup>2</sup>, Frank G van Steenbeek<sup>1</sup>, Manon Bouwmeester<sup>1</sup>, Roos-Anne Samsom<sup>1</sup>, Marit Keuper-Navis<sup>3</sup>, Thomas K van der Made<sup>4</sup>, Daniel Kogan<sup>3</sup>, Sarah Braem<sup>3</sup>, Luc J W van der Laan<sup>5</sup>, Hossein Eslami Amirabadi<sup>6</sup>, Evita van de Steeg<sup>3</sup>, Rosalinde Masereeuw<sup>4</sup> and Bart Spee<sup>1</sup>

- Department of Clinical Sciences, Faculty of Veterinary Medicine, Utrecht University, Utrecht, The Netherlands
- <sup>2</sup> Institute for Risk Assessment Sciences (IRAS), Utrecht University, Utrecht, The Netherlands
- Department of Metabolic Health Research, Netherlands Organisation for Applied Scientific Research (TNO), Leiden, The Netherlands
- <sup>4</sup> Division of Pharmacology, Department of Pharmaceutical Sciences, Faculty of Science, Utrecht University, Utrecht, The Netherlands
- Department of Surgery, Erasmus MC Transplant Institute, University Medical Center Rotterdam, Rotterdam, The Netherlands
- AZAR Innovations, Utrecht, The Netherlands
- \* Author to whom any correspondence should be addressed.

E-mail: adam.myszczyszyn@gmail.com

**Keywords:** bioengineering, drug metabolism and transport, liver, organoids, organs-on-a-chip, pharmacokinetics, stem cells Supplementary material for this article is available online

### **Abstract**

Liver-on-a-chip models predictive for both metabolism, and blood and canalicular transport of drug candidates in humans are lacking. Here, we established a bioengineered and 3Rs-complied (animal component-free) hepatocyte-like millifluidic system based on 3D hollow fiber membranes (HFMs), recombinant human laminin 332 coating and adult human stem cell-derived organoids. Organoid fragments formed polarized and tight monolayers on HFMs with improved hepatocyte-like maturation, as compared to standard 3D organoid cultures in Matrigel from matched donors. Gene expression profiling and immunofluorescence revealed that hepatocyte-like monolayers expressed a broad panel of phase I (e.g. CYP3A4, CYP2D6, CYP2C9) and II (e.g. UGTs, SULTs) drug-metabolizing enzymes and drug transporters (e.g. MDR1, MRP3, OATP1B3). Moreover, statically cultured monolayers displayed phase I and II metabolism of a cocktail of six relevant compounds, including midazolam and 7-hydroxycoumarin. We also demonstrated the disposition of midazolam in the basal/blood-like circulation and apical/canalicular-like compartment of the millifluidic chip. Finally, we studied the bioavailability of midazolam and coumarin on-a-chip in combination with a small intestine-like system. In conclusion, we generated a proof-of-concept liver organoid-on-a-chip model for examining metabolism and transport of drugs, which can be further developed to predict pharmacokinetics (PK)/absorption, distribution, metabolism and excretion (ADME) profiles in humans.

### 1. Introduction

Rodent models used during preclinical development are poorly predictive for behaviors of drug candidates in humans [1], and the lack of translation results in 90% failure of those compounds during clinical development [2]. This problem was acknowledged by the US Food and Drug Administration (FDA) Modernization Act 2.0 of 2022 that allows for utilizing

relevant *in vitro* models instead of animal testing for every new non-clinical drug development protocol [3]. The lack of predictiveness for pharmacokinetics' (PK) parameters in humans, *i.e.* absorption, distribution, metabolism and excretion (ADME), is the second major biological reason for high attrition rates of drug candidates in phase I of clinical development, after safety [1, 4]. This underscores the need for more predictive *in vitro* preclinical systems

for major PK/ADME-related organs such as the liver.

In the past years, advanced, bioengineered organon-a-chip (microphysiological) technologies have emerged as most promising in vitro models for predicting human PK/ADME profiles, as they can closely recapitulate the architecture, environmental factors and functions of tissues of origin [5-7]. Based on commercially manufactured chips (from CN Bio Innovations Ltd.; Emulate, Inc.; Javelin Biotech, Inc.; and TissUse GmbH), these micro- and millifluidic technologies improved the functionality of primary human hepatocytes (PHHs) over a longer period of culture by recapitulating their native canalicular polarization thanks to extracellular matrix (ECM) sandwich-culture or 3D/spheroid growth as well as by incorporating supporting cells, vasculature and flow-induced mechanical forces [8-12]. However, this makes PHHs-on-a-chip systems only suitable for studying drug uptake and metabolism, as the apical/canalicular-like compartment between cells is inaccessible for examining passive diffusion (transcellular and paracellular) and active transport of drugs and their metabolites [13]. Thus, liver-on-achip models with an apical/canalicular-like compartment that can be directly sampled to capture biliary excretion and enterohepatic circulation of drug candidates are an unmet need [5, 7]. Previously, human embryonic stem cell (ESC)- and induced pluripotent stem cell (iPSC)-derived hepatocytelike monolayers on Transwell membranes displayed columnar epithelial polarization with an accessible apical/canalicular-like compartment. Though, perfusion was not applied, and these hepatocyte-like cells were still immature, as they exhibited transcriptomic profiles similar to the embryonic liver [14].

Hollow fiber membranes (HFMs) have emerged as perfusable scaffolds that are suitable for generating polarized epithelial monolayers with two accessible micro-/millifluidic compartments. These 3D tubular-shaped and porous membranes are made of a biocompatible, stable and low-cost material such as MicroPES (polyethersulfone) [15]. In contrast to flat 2D Transwell membranes, HFMs were shown to enhance cell differentiation [16], possibly thanks to 3D geometrical properties [17]. Previously, we took advantage of HFMs to establish kidney proximal tubule-[18] and small intestine-on-a-chip [15] systems based on immortalized human cell lines. In addition, we created mouse [19] and human [20] bile duct-on-a-chip HFM-based models using liver organoids. However, an organoid-derived HFMbased liver-on-a-chip system has not been reported to

Human stem cell-derived 3D organoids from the healthy adult liver, so-called intrahepatic cholangiocyte organoids (ICOs) [21], are a robust cell source for establishing liver-on-a-chip systems. ICOs can

be expanded in Matrigel droplet-based cultures in expansion medium via serial passaging over a long-term while retaining genetic stability and potential for biobanking. They are enriched in LGR5-positive bipotent progenitor cells that can maturate into hepatocyte-like cells upon a switch to a differentiation medium. These cells maintain major functional features of individuals, including variations in the expression of metabolizing enzymes and transporters of drugs [22].

Current liver-on-a-chip models do not meet the 3Rs' principles [3], as they utilize fetal bovine serumrich media and animal-derived ECM components such as Matrigel from mouse sarcoma, rat tail collagen I and bovine fibronectin [9]. These components are undefined, which results in experimental variability, poor reproducibility and the lack of standardization of liver-on-a-chip systems, potentially blocking their approval by regulatory agencies [3]. Alternative human tissue extract-derived ECM components like collagen IV from placenta [9] are not fully defined and are also quite costly. In contrast, recombinant human laminins such as laminin 111, 332 and 511 can aid animal component-free standardization and are more cost effective. Moreover, these laminins are expressed in the quiescent [23] and regenerating [24] adult human liver, and were shown to maintain the functionality of 2D monolayer cultures of PHHs [23] as well as to drive hepatocyte-like differentiation of ESCs [25, 26] and iPSCs [27–29]. Previously, we demonstrated that a chemically defined synthetic hydrogel, PIC, and laminin 111 can replace Matrigel in culturing ICOs [30, 31]. Together, recombinant human laminins can offer a biologically relevant alternative for ECM components in liver-on-a-chip systems.

3Rs-complied (animal component-free) liver-ona-chip models that display improved maturation and tight epithelial barriers with apical-to-basolateral columnar polarization are necessary for a successful human in vitro-to-in vivo extrapolation (IVIVE) of PK/ADME profiles of drug candidates. Here, we generated a bioengineered hepatocyte-like millifluidic system based on HFMs, recombinant human laminin 332 coating, human liver organoid fragments and serum-free media with defined growth factors. This system is metabolically active and allows for the sampling of the basal and apical compartment to examine transport of parent compounds and their metabolites across polarized cell monolayers. Thus, our proof-of-concept model has application potential in determining experimental PK/ADME kinetic values of drug candidates.

### 2. Method

### 2.1. Liver organoids

Tissue from healthy adult liver transplant donors at the Erasmus Medical Center Rotterdam (EMC,

The Netherlands) was used. These included: donor 1 (male, middle-aged), donor 2 (female, middleaged), donor 3 (male, middle-aged), donor 4 (female, middle-aged) and donor 5 (female, middle-aged). ICOs were established, as described previously [22, 32]. ICOs were cultured in 25  $\mu$ l droplets of Growth Factor Reduced Matrigel (Corning), 70% (v/v; in expansion medium, EM) and 100% for batches  $\geqslant 9$  mg ml<sup>-1</sup> and  $\leqslant 9$  mg ml<sup>-1</sup> of proteins, respectively. Matrigel droplets with ICO fragments were cultured in EM that contained advanced DMEM/F12 (Thermo Fisher Scientific), 1% (v/v) penicillin-streptomycin (Thermo Fisher Scientific), 1% (v/v) GlutaMAX (Thermo Fisher Scientific), 10 mM HEPES (Thermo Fisher Scientific), 2% (v/v) B27 supplement without vitamin A (serumfree, Thermo Fisher Scientific), 1% (v/v) N2 supplement (serum-free, Thermo Fisher Scientific), 1.25 mM N-acetylcysteine (Sigma-Aldrich), 10 mM nicotinamide (Sigma-Aldrich), 2% (v/v) human Rspondin-3-Fc Fusion Protein Conditioned Medium (ImmunoPrecise Antibodies), 50 ng ml<sup>-1</sup> recombinant human EGF (Peprotech), 100 ng ml<sup>-1</sup> recombinant human FGF10 (Peprotech), 25 ng ml<sup>-1</sup> recombinant human HGF (Peprotech), 10 nM human gastrin (Leu15 analog, AnaSpec), 5  $\mu$ M A83-01 (STEMCELL Technologies) and 10  $\mu$ M forskolin (Sigma-Aldrich). Cultures were incubated in a humidified atmosphere at 37 °C and 5% CO<sub>2</sub>. EM was refreshed every 2–3 d. Cultures were passaged every 4-7 d (until the confluency was reached) at a 1:3-1:5 split ratio by mechanical fragmentation. Passages 4-12, were used for experiments. To induce hepatocyte-like maturation, ICOs expanded for 4-7 d were further cultured for 3 d in pre-differentiation medium (pre-DM), i.e. EM supplemented with 25 ng ml<sup>-1</sup> recombinant human BMP7 (Peprotech), and for 7 d in differentiation medium (DM) consisting of advanced DMEM/F12 (Thermo Fisher Scientific), 1% (v/v) penicillin-streptomycin (Thermo Fisher Scientific), 1% (v/v) GlutaMAX (Thermo Fisher Scientific), 10 mM HEPES (Thermo Fisher Scientific), 2% (v/v) B27 supplement without vitamin A (serum-free, Thermo Fisher Scientific), 1% (v/v) N2 supplement (serum-free, Thermo Fisher Scientific), 1.25 mM Nacetylcysteine (Sigma-Aldrich), 50 ng ml<sup>-1</sup> recombinant human EGF (Peprotech),  $100 \text{ ng ml}^{-1}$  recombinant human FGF19 (Peprotech), 25 ng ml $^{-1}$ recombinant human HGF (Peprotech), 25 ng ml<sup>-1</sup> recombinant human BMP7 (Peprotech), 10 nM human gastrin (Leu15 analog, AnaSpec), 0.5  $\mu$ M A83-01 (STEMCELL Technologies), 10 μM DAPT (Selleck Chemicals) and 30  $\mu M$  dexamethasone (Sigma-Aldrich). For gene expression profiling, ICOs were cultured in DM for 10 d without the pre-DM phase. DM was refreshed every 2-3 d. Brightfield

images were acquired with an EVOS M5000 Imaging System (Thermo Fisher Scientific). All the organoid lines were Mycoplasma-free. Tests were performed every three months, according to an institute's protocol.

### 2.2. A hepatocyte-like HFM-based system

MicroPES (polyethersulfone) TF10/PVP HFMs with an internal diameter of 300  $\mu$ m, wall thickness of 100  $\mu$ m and a maximum pore size of 0.5  $\mu$ m were extracted from a SepaPlas 06 plasma filter (MEDICA) and cut into 3- or 4 cm pieces for static and chip assays, respectively. HFM pieces were then sterilized in 70% (v/v) EtOH for 30 min on a roller and washed 3x with sterile 1x PBS. L-DOPA (3,4-dihydroxy-L-phenylalanine, Sigma-Aldrich) was dissolved to  $2 \text{ mg ml}^{-1}$  in 10 mM Tris-HCl buffer (pH 8.5) on a carousel (at 10 rpm) at 37 °C overnight. The solution was filter-sterilized and added to sterile HFM pieces that were then incubated on a carousel (at 10 rpm) at 37 °C for four hrs. Next, the solution was aspirated, and L-DOPA-coated HFM pieces were washed 3x with sterile 1x PBS and stored at 4 °C for one week or used immediately for ECM coating. For static assays, Growth Factor Reduced Matrigel (Corning), or recombinant human laminin 111, 211, 332, 411 or 511 (BioLamina) were diluted with sterile 1x PBS to 10  $\mu$ g ml<sup>-1</sup> (according to the manufacturer's recommendation) in the volume of 5 ml in 5 ml Protein LoBind tubes (Eppendorf). For chip assays, laminin 332 was used exclusively. Up to 15 HFM pieces were transferred to an ECM solution and incubated on a carousel (10 rpm) at 37 °C for two hrs. ECMcoated HFM pieces were immediately used for seeding ICO fragments. Matrigel droplets with ICOs were mechanically harvested using advanced DMEM/F12 (Thermo Fisher Scientific) with 1% (v/v) penicillinstreptomycin (Thermo Fisher Scientific), 1% (v/v) GlutaMAX (Thermo Fisher Scientific) and 10 mM HEPES (Thermo Fisher Scientific), and Matrigel was removed by repeated pipetting and washings. ICO pellets were mechanically fragmented by extensive pipetting in 1 ml of the latter medium. For static assays, HFM pieces were seeded with ICO fragments in 2 ml tubes at a ratio of two pieces per 1 ml of EM with ICO fragments harvested from eight confluent Matrigel droplets. For chip assays, single HFM pieces were placed in an in-house 3D-printed holder using a biocompatible resin [33] and fixed with dental glue (Gi-Mask Automix, Coltène). The holder was designed in SolidWorks (Dessault Systèmes) and stereolitography-printed using a RapidShape S60 LED DLP printer (Rapid Shape). The design is the subject of a patent process. HFM-carrying holders were seeded with ICO fragments in 5 ml tubes at a ratio of one holder per 3.5 ml of EM with ICO fragments harvested from 28 confluent Matrigel droplets.

For static assays, tubes were incubated horizontally in a humidified atmosphere at 37 °C and 5% CO<sub>2</sub> with a gentle resuspension by a 360° rotation every 45 min (4x), totalling four hrs of incubation. Next, cell-laden HFMs were transferred to 6-well plates with 2 ml of EM (one HFM per well) and cultured for 4-7 d in a humidified atmosphere at 37 °C and 5% CO<sub>2</sub> without medium change, until the confluency was reached. For chip assays, tubes were incubated vertically on a carousel (at <0.5 rpm) at 37 °C for four hrs. Cell-laden HFMs in holders were transferred to 6-well plates with 6 ml of EM (one holder per well) and cultured for 4-7 d in a humidified atmosphere at 37 °C and 5% CO<sub>2</sub>, without medium change, until the confluency was reached. To induce hepatocyte-like maturation, HFM-expanded monolayers were further statically cultured for 3 d in pre-DM and for 7 or 14 or 21 d in DM. HFM-expanded monolayers in holders were further statically cultured for 3 d in pre-DM and for 7 d in DM. Brightfield images were acquired with an EVOS M5000 Imaging System (Thermo Fisher Scientific).

### 2.3. Real-time qPCR

Matrigel droplets with ICOs (eight per condition) were harvested, and Matrigel was removed by incubating with Cell Recovery Solution (Corning), according to the manufacturer's instructions. Total RNA was isolated from HFM-grown monolayers (six per condition), ICOs and liver tissue specimens using the RNeasy Mini Kit (Qiagen), according to the manufacturer's instructions, including supplementing RLT buffer with  $\beta$ -mercaptoethanol and treatment of lysates with DNase I. RNA was quantified using a D-1000 NanoDrop spectrophotometer (Thermo Fisher Scientific). 1  $\mu$ g RNA was reverse-transcribed into cDNA using the iScript cDNA synthesis kit (Bio-Rad), according to the manufacturer's instructions. Synthesized cDNA was diluted 7x. Relative mRNA of genes of interest was quantified by real-time qPCR reactions performed in a CFX384 Touch Real-Time PCR Detection System (thermal cycler, Bio-Rad). The iQ SYBR Green Supermix (Bio-Rad) and 0.7  $\mu$ M primers were used (table 1) that were designed inhouse and synthesized at Eurogentec, and then validated by performing a temperature gradient analysis. A 2-step reaction was performed at 60 °C, i.e. combined annealing and elongation, with 39 cycles. Primer specificity was tested by melting curve analysis and running reactions with a negative control (without cDNA). Primer efficiency was tested by running standard curves with pooled cDNA samples. Relative mRNA expression values were normalized to the averaged endogenous controls RPL19 (structural protein) and HPRT (metabolic enzyme) using the  $2^{-\Delta\Delta Ct}$  method. A cut-off  $C_a$  value was 35.

### 2.4. Bulk mRNA sequencing

Matrigel droplets with ICOs (eight per condition) were mechanically harvested, and Matrigel was removed by incubating with Cell Recovery Solution (Corning), according to the manufacturer's instructions. Total RNA was isolated from HFM-grown monolayers (six per condition), ICOs and liver tissue specimens using the RNeasy Mini Kit (Qiagen), according to the manufacturer's instructions, including supplementing RLT buffer with  $\beta$ mercaptoethanol and treatment of lysates with DNase I. The amount and quality of RNA was measured with the Agilent RNA 6000 Nano Kit and an Agilent 2100 Bioanalyzer (Agilent Technologies), according to the manufacturer's instructions. All samples had a RNA integrity number value of ≥8. A minimum of 50  $\mu$ l RNA at a minimum concentration of 4 ng  $\mu$ l<sup>-1</sup> (200 ng in total) was submitted for mRNA library preparation (Truseq RNA stranded polyA enrichment) and sequencing at the Utrecht Sequencing Facility, according to internal protocols. The libraries were sequenced using the NextSeq2000 platform (Illumina), producing  $1 \times 50$  bp reads, ~20 M reads per sample, 1000 M reads per flow cell (P3, 50 cycles)[34]. ICO and liver tissue samples were sequenced separately from monolayer samples. mRNA reads were aligned to the human reference genome GRCh37 using the STAR software version 2.4.2a (https://github.com/UMCUGenetics/ RNASeq-NF/). Datasets were corrected for batch effects using Combat\_seq [35] and normalized for library size using trimmed mean of M values (TMM) [36]. Fold changes were calculated in edgeR [37]. For comparisons of gene expression, the exact test was used to calculate P-values that were corrected for the false discovery rate (FDR) of 5% using the Benjamini-Hochberg method. Genes were considered differentially expressed at adjusted P-value <0.05. The principal component analysis plot and heatmaps of differentially expressed genes were created using ggplot2 [38]. For the functional annotation, The Database for Annotation, Visualization and Integrated Discovery (DAVID) was used (https:// david.ncifcrf.gov/). Differentially expressed genes were subjected to a cut-off for both adjusted *P*-value <0.05 and log2 fold change  $\ge 2$  (actual fold change ≥4) for monolayers DM 7 d over organoids DM 10 d (upregulation in monolayers). 383 genes were selected. Using the entire human (Homo sapiens) genome as a background for the ENSEMBL\_GENE\_ID identifier, 350 genes (IDs) were identified and analyzed. Default parameters were used, except for the Enrichment Thresholds (EASE Scores, modified Fisher-exact P-values) and adjusted P-values (Benjamini-Hochberg correction) that were subjected to the cut-off of <0.05 for all terms in each of 59 clusters. By this, 18 clusters were determined.

Table 1. Primer sequences for real-time qPCR.

Gene	Forward primer 5'-3'	Reverse primer 5'-3'		
RPL13A	GTGAAGGCATCAACATTTCTG	GATAGGCAAACTTTCTTGTAGG		
HPRT	TATTGTAATGACCAGTCAACAG	GGTCCTTTTCACCAGCAAG		
ALB	GTTCGTTACACCAAGAAAGTACC	GACCACGGATAGATAGTCTTCTG		
CYP3A4	TGATGGTCAACAGCCTGTGCTGG	CCACTGGACCAAAAGGCCTCCG		
CYP2D6	GAGGTGCTGAATGCTGTC	AGGTCATCCTGTGCTCAG		
CYP2C9	GACAGAGACGACAAGCAC	AATCACACGTTCAATCTCTTCC		
CYP2B6	CTACCAAGATCAAGAGTTCCTG	ATTTCAAGAAGCCAGAGAAGAG		
UGT2A3	AATACTCGGCTGTATGATTGG	CATAGATCCCATTCATTCCACC		
SULT1A1	TTCCTTGAGTTCAAAGCCC	TGTCTTCAGGAGTCGTGG		
ABCB1 (MDR1)	CAGTGGCTCACACCCGTAATC	GCCAGGCTGGTCTTGAACTC		
ABCC3 (MRP3)	GTCCGCAGAATGGACTTGAT	TCACCACTTGGGGATCATTT		

### 2.5. Immunofluorescence microscopy

For whole-mount immunofluorescence, HFMgrown monolayers were washed once in 1x PBS, fixed in 4% (v/v) paraformaldehyde (PFA) on a roller at 4 °C for 45 min. Next, PFA was removed and monolayers were washed 3x in 1x PBS. Monolayers were cut into 1 cm (or 1.5 cm) pieces and blocked on a rocker at room temperature (RT) for one h in a dilution/washing buffer containing 1x PBS, 1% (w/v) BSA and 0.1% (v/v) Tween 20 that was supplemented with 10% (v/v) goat serum (Sigma-Aldrich). Monolayer pieces were then incubated with primary antibodies in the buffer on a rocker in the darkness at 4 °C overnight. These included rabbit anti-ZO1 (1:50, Thermo Fisher Scientific, 40-2300), rabbit anti-HNF4α (1:50, Novus Biologicals, NBP1-89679), rabbit anti-OATP1B3 (1:50, Novus Biologicals, NBP1-80980), rabbit anti-OCT1 (1:50, Novus Biologicals, NBP1-59464), mouse anti-MDR1 (1:50, Santa Cruz Biotechnology, sc-55510), rabbit anti-MRP2 (1:50, Abcam, ab187644), rabbit anti-MRP3 (1:50, Novus Biologicals, NBP2-37923), mouse anti-BCRP (1:50, Santa Cruz Biotechnology, sc-377176) and phalloidin (a toxin against F-actin) conjugated to Alexa Fluor 488 (1:400, Thermo Fisher Scientific, A12379). Next, monolayer pieces were washed in the buffer 3x for 20 min on a rocker in the darkness. Incubation with secondary antibodies in the buffer, i.e. goat anti-rabbit-Alexa Fluor 488 (1:100, Thermo Fisher Scientific, A11008) and goat anti-mouse-Alexa Fluor 488 (1:100, Thermo Fisher Scientific, A11029), and with DAPI (1  $\mu$ g ml<sup>-1</sup>, Thermo Fisher Scientific) was performed for two hrs on a rocker in the darkness at RT. Then, monolayer pieces were washed in the buffer 3x for 10 min on a rocker in the darkness, followed by mounting on Lab-Tek II Chambered Coverglass (Nunc) with ProLong Diamond Antifade Mountant (Thermo Fisher Scientific) and immediate imaging. For immunofluorescence of paraffin sections, confluent HFM-grown monolayers were washed once in 1x PBS, fixed in 4% (v/v) PFA on a roller at 4 °C for 45 min. Next, PFA was removed and monolayers were washed 3x in 1x PBS. Monolayers were cut into 0.5 cm pieces and mounted vertically in 2.5% (w/v) agarose droplets. Agarose droplets were dehydrated overnight in 70% (v/v) EtOH, 96% (v/v) EtOH, 100% (v/v) EtOH and Xylene, and embedded in paraffin. Paraffin blocks were cut into 5  $\mu$ m slices using a HistoCore MULTICUT microtome (Leica Biosystems). Paraffin slices were incubated on a heating plate at 60 °C for 30 min, and rehydrated in Xylene (2x 5 min), 100% EtOH (2x 5 min), 96% EtOH (2x 3 min), 70% EtOH (2x 3 min) and water (2x 3 min), followed by antigen retrieval in TRIS-EDTA buffer (pH 9) at 95 °C for 30 min. Slices were then washed in 1x PBS 3x for 5 min and blocked in the buffer with 10% (v/v) goat serum (Sigma-Aldrich) in a humified chamber at RT for one h. Next, slices were incubated with primary antibodies in the buffer in a humified chamber at 4 °C overnight. These included mouse anti-E-CAD (1:50, BD Biosciences, 610181), rabbit anti-Villin (1:50, Novus Biologicals, NBP1-85335) and rabbit anti-NTCP (1:50, Novus Biologicals, NBP1-60109). After that, slices were washed in 1x PBS with 0.1% (v/v) Tween 20 3x for 10 min and incubated with secondary antibodies in the buffer, i.e. goat anti-mouse-Alexa Fluor 488 (1:100, Thermo Fisher Scientific, A11029) and goat anti-rabbit-Alexa Fluor 647 (1:100, Thermo Fisher Scientific, A21245), and with DAPI (1  $\mu$ g ml<sup>-1</sup>, Thermo Fisher Scientific) in a humified chamber in the darkness at RT for one h. Then, slices were washed in 1x PBS with 0.1% (v/v) Tween 20 3x for 10 min in the darkness, followed by mounting on Superfrost Plus slides (Thermo Fisher Scientific) with ProLong Diamond Antifade Mountant (Thermo Fisher Scientific) and #1,5 thickness (0,17 mm) cover glass, and immediate imaging. For imaging, an inverted Leica TCS SP8 confocal microscope and the LAS X software (Leica Microsystems) were used. Laser power of 70% was applied. The frame or stack sequential mode from the dye assistant for DAPI, Alexa Fluor 488 and Alexa Fluor 674 was used for excitation and detection without crosstalk between the channels. The detectors used were PMT for DAPI and HyD for Alexa Fluor 488 and Alexa Fluor 647. The objectives used were HC PL FLUOTAR L 20x/0.40 DRY or HC PL APO 40x/0.95 DRY. Images were acquired using the acquisition mode xyz, a pinhole 1 airy unit, format 2048 × 2048 and speed 100. Line average 2-4 for a strong but blurry signal, and line accumulation 2-4 for a weak but sharp signal were applied. An inverted Leica Thunder DMi8 fluorescence microscope and the LAS X software (Leica Microsystems) were used to generate and merge tile scans of entire whole-mount-stained 1.5 cm HFM pieces. Excitation and detection were applied for DAPI and Alexa Fluor 488. The objective used was HC PL FLUOTAR 10x/0.32 DRY. A computational clearing was applied.

### 2.6. A calcein-AM assay

To examine the confluency of HFM-grown monolayers, the system was incubated with 1  $\mu$ M calcein-AM (Santa Cruz Biotechnology) in EM in a humidified atmosphere at 37 °C and 5% CO<sub>2</sub> for 15 min. Monolayers were washed 3x in EM and immediately imaged using the FITC channel of an EVOS M5000 Imaging System (Thermo Fisher Scientific). For the functional efflux assay, differentiated monolayers was pre-incubated in DM with 10  $\mu$ M PSC-833, 10  $\mu$ M KO-143 and 50  $\mu$ M MK-571 (Selleck Chemicals) or with an equivalent amount of DMSO (Sigma-Aldrich) in a humidified atmosphere at 37 °C and 5% CO<sub>2</sub> for one h. Then, monolayers were incubated in DM with the inhibitors or DMSO and with 1  $\mu$ M calcein-AM in a humidified atmosphere at 37 °C and 5% CO<sub>2</sub> for 15 min. Monolayers were washed 3x in DM and immediately imaged using the FITC channel of an EVOS M5000 Imaging System (Thermo Fisher Scientific). The fluorescence was quantified using the ImageJ software (https://imagej.net/ij/).

### 2.7. Chip assays

A biochamber was printed in-house in the same way as the holder. The design is also the subject of a patent process. The holder carrying HFM-grown monolayers was washed once in HBSS (with calcium, magnesium, glucose and sodium bicarbonate; pH 7–7.4; Thermo Fisher Scientific) supplemented with 1% (v/v) GlutaMAX, 10 mM HEPES and 1 mM sodium pyruvate (Thermo Fisher Scientific), then placed in the biochamber and sealed with rubber O-rings. 710  $\mu$ l buffer was added to the apical compartment of the biochamber, and sampling ports were sealed with luer locks. For 10 min perfusion (basal flow-through), the biochamber was placed on a heating plate at 37 °C and connected to an Ismatec IPC peristaltic pump (Masterflex) using the essential Slang TYGON LMT-55 (PVC; internal diameter 0.51 mm, outer diameter 2.31 mm; Roth) tubing and an additional short tubing (silicone; internal diameter 1.65 mm,

outer diameter 3.35 mm; Avantor). For 3 h perfusion (basal circulation), the two latter types of tubing were used together with an additional Teflon tubing (internal diameter 1 mm, outer diameter 3 mm; 2700, Rubber) to minimize unspecific binding of hydrophobic compounds. For 3 h perfusion, a subsampling of 200 or 400  $\mu$ l circulation buffer was performed and 200 or 400  $\mu$ l fresh buffer was added. After perfusion, the biochamber was disassembled, and fluids from the apical compartment and basal circulation were collected for the quantification of the compounds using LC-MS/MS or for the quantification of FITC-dextran (FD4, 4000 g mol<sup>-1</sup>, 50  $\mu$ M; Sigma-Aldrich) fluorescence. For the FD4 fluorescence quantification, 100  $\mu$ l fluid was added to a 96well black-walled plate (Agilent) and measured using the FITC channel of a CLARIOstar Plus multi-mode microplate reader (BMG LABTECH). Intrinsic clearance of midazolam (CLint) and apparent permeability  $P_{\rm app}$  of FD4 were calculated using standard formulas [33, 39]. Small intestine-like organoid monolayers were cultured on Transwell membranes, as described previously [40]. Monolayers were exposed on the apical/luminal-like side. Basal effluents were collected after one and two hrs, and combined for subsequent perfusion of the hepatocyte-like system for three hrs. To further minimize the unspecific binding of hydrophobic compounds during 3 h perfusion (in addition to the Teflon tubing), the system was first saturated overnight with the buffer containing the parent dose of each compound.

### 2.8. Liquid chromatography-mass spectrometry/mass spectrometry (LC-MS/MS)

The drug-metabolizing activity of HFM-grown monolayers and ICOs was evaluated using a cocktail of parent compounds, as described previously [32]. These included 5  $\mu$ M midazolam (BUFA; metabolites: 1'-hydroxymidazolam, Sigma-Aldrich; 1'-hydroxymidazolam glucuronide, LGC Standards), 15 µM dextromethorphan (Santa Cruz Biotechnology; metabolite: dextrorphan tartrate, Sigma-Aldrich), 20 μM tolbutamide (Sigma-Aldrich; metabolite: 4-hydroxytolbutamide, LGC Standards), 15  $\mu$ M phenacetine (Sigma-Aldrich; metabolite: acetaminophen, Sigma-Aldrich), 20 µM bupropion-HCl (Sigma-Aldrich; metabolite: hydroxybupropion, Sigma-Aldrich) and 12  $\mu$ M 7-hydroxycoumarin (umbelliferone, Sigma-Aldrich; metabolite: 7hydroxycoumarin glucuronide, LGC Standards). Differentiated monolayers and organoids (7 d) were exposed to the cocktail in DM in a humidified atmosphere at 37 °C and 5% CO2 for 24 h. Collagen I sandwich PHHs were previously cultured for 48 h and then exposed for four hrs [32], and data were extracted and normalized. For organoids and PHHs, 1'hydroxymidazolam glucuronide was not measured.

For liver-on-a-chip experiments, 5  $\mu$ M midazolam in the buffer was used. For dual-organ-on-a-chip system experiments, hepatocyte-like and Transwell monolayers were exposed to 50 µM midazolam and 50  $\mu$ M coumarin (Sigma-Aldrich) in the buffer. For a CYP3A4 inhibition assay, HFM-grown monolayers were incubated in DM with 10  $\mu$ M ketoconazole (Selleck Chemicals) or an equivalent amount of 100% (v/v) EtOH for three hrs and then in DM with 1  $\mu$ M ketoconazole or EtOH and 5  $\mu$ M midazolam for 24 h. 200  $\mu$ l of culture medium or buffer were collected in the 1.5 ml Short Thread Vials with the ND9 Short Thread Screw Caps (BGB Analytik) containing 200 µl ultrapure MeOH, vortexed and stored at -20 °C until the quantification of the parent compounds and metabolites using LC-MS/MS. As described previously [32], samples were centrifuged for 10 min at 1500 g to precipitate any protein prior to the analysis. Standards of the parent compounds and metabolites were prepared in the same matrix (medium or buffer) as samples. Usually, 1  $\mu$ l medium or buffer with MeOH was injected. If necessary, selected metabolites were quantified using a high sensitivity method with a 5  $\mu$ l injection. Standards and samples were analyzed in a single run using a Shimadzu triple-quadrupole LCMS 8050 system with two Nexera XR LC-20AD pumps, a Nexera XR SIL-20AC autosampler, a CTO-20AC column oven and an FCV-20AH2 valve unit (Shimadzu). The compounds were separated on a Synergi Polar-RP column (150  $\times$  2.0 mm, 4  $\mu$ m, 80 Å) with a 4  $\times$  2 mm C18 guard column (4  $\times$  2 mm, Phenomenex). The mobile phase consisted of 0.1% (v/v) formic acid in ultrapure water (A) and 0.1% (v/v) formic acid in MeOH (B), and was set as 100% A (0-1 min), 100% to 5% A (1-8 min), 5% A (8-9 min), 5% to 100% A (9-9.5 min) and 100% A (9.5-12.5 min). The total run time was 12.5 min, and the flow rate was 0.2 ml min<sup>-1</sup>. Peaks were integrated using the LabSolutions software (Shimadzu). For each compound, a limit of quantification (LOQ) was determined based on a standard curve and a limit of detection (LOD) was determined based on a noise signal. For each sample set, a dose (time 0 h) and a blank (a negative control) were measured. For each parent compound and its metabolite(s), data were normalized to an actual (measured) dose in the relation to an expected (calculated) dose. Intracellular levels of the parent compounds and metabolites were not taken into account.

### 2.9. Statistical analysis

All statistical analyses were performed using the Microsoft Excel (Microsoft) and GraphPad Prism software (GraphPad), unless otherwise stated. All data are presented as mean  $\pm$  SD (error bars) with

individual independent (donors) or technical replicates marked, unless otherwise stated. Statistical details of experiments can be found in figure legends.

### 3. Results

### 3.1. Organoid fragments form polarized hepatocyte-like monolayers on laminin 332-coated HFMs

To enable the formation of cell monolayers, HFMs were coated with biological polymeric glue, L-DOPA, that facilitates subsequent coating with ECM components [15, 18-20]. To replace animal-derived and undefined ECM components such as Matrigel, we examined full-length recombinant human laminins that represent the entire spectrum of  $\alpha$ 1-5 chains crucial for binding to respective integrins, i.e. laminin 111, 211, 332, 411 and 511 [41]. Coated HFMs were seeded with fragments of organoids that were grown in expansion medium in standard Matrigel dropletbased cultures (figure S1(A)) and can be matured into hepatocyte-like cells upon a switch to differentiation medium [22] (figure S1(B)). Only organoid fragments grown on laminin 332- and 511-coated HFMs succeeded in generating confluent monolayers over 7 d (figure S2(A)). Upon differentiation, the expression of crucial functional markers of mature hepatocytes, i.e. ALB (albumin), phase I CYP450 (CYP3A4, CYP2D6, CYP2C9, CYP2B6) and phase II glucuronosyltransferase/UGT and sulfotransferase/SULT (UGT2A3, SULT1A1) drug-metabolizing enzymes as well as apical ABCB1 (MDR1) and basolateral ABCC3 (MRP3) drug transporters was upregulated in monolayers grown on laminin 332-coated HFMs, as compared to laminin 511-coated HFM-grown monolayers and Matrigel organoid cultures from matched donors (figure S2(B)). However, the expression for ALB, CYP2D6 and CYP2B6 was downregulated in laminin 332-coated HFM-grown monolayers versus the whole adult liver from matched donors. As laminin 332 drives both efficient expansion and maturation, it was selected for further developments (figure 1(A)).

We did not observe any morphological changes when differentiated monolayers were monitored for 7, 14 and 21 d (figure 1(B)), demonstrating the potential for long-term studies. A 3D reconstruction revealed that monolayers were intact (figure 1(C)). In addition, we detected a ubiquitous presence of cytoskeleton-associated F-actin (figures 1(D) and S3) and tight junction-associated ZO1 (figure 1(E)) in cell membranes. To enable passive diffusion (transcellular and paracellular) and active transport of drugs [13] between two microfluidic compartments, monolayers must form columnar tubular epithelium with apical-to-basolateral polarization, as opposite to the native hepatic canalicular architecture with

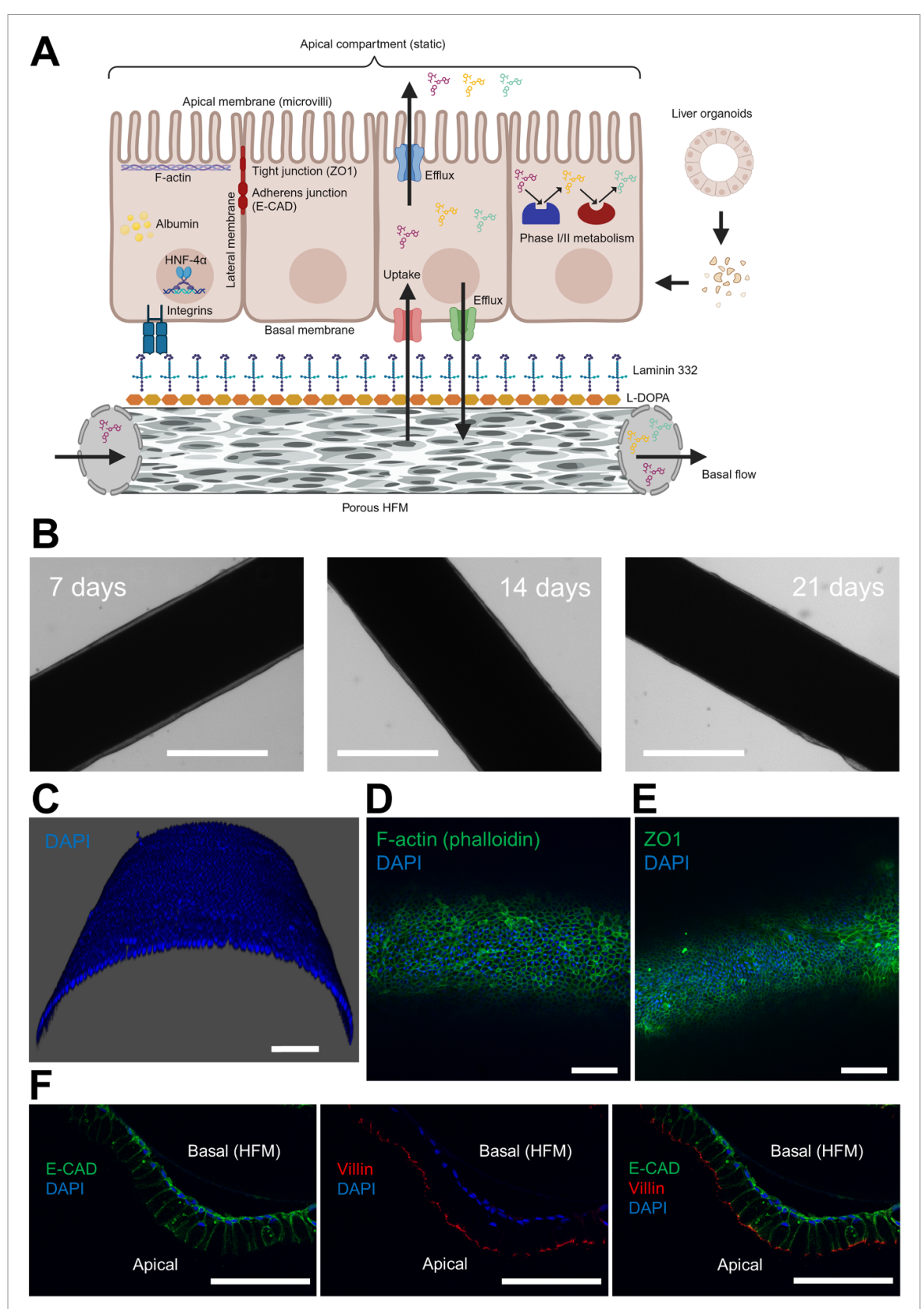


**Figure 1.** Establishing hepatocyte-like HFM-grown monolayers optimized for organ-on-a-chip assays. (A) A scheme showing a minimal viable product for the liver-on-a-chip system. (B) Representative brightfield images of confluent monolayers (a median section) after 3 d in pre-DM, and 7, 14 and 21 d in DM under the static culture. (C) A representative 3D-reconstituted whole-mount confocal immunofluorescence microscopy image of a HFM-grown monolayer (an anterior-dorsal section) after 7 d in DM. (D) A representative whole-mount confocal immunofluorescence microscopy image of F-actin (phalloidin) in a dorsal section of a HFM. (E) A representative whole-mount confocal immunofluorescence microscopy image of ZO-1 in a dorsal section of a HFM. (F) A representative confocal immunofluorescence microscopy image for the basolateral localization of E-CAD and the apical localization of Villin in cell membranes of a monolayer in an anterior section of a HFM. Data information: scale bars; in B, 500  $\mu$ m; in (C)–(F), 100  $\mu$ m. In (A), the scheme was created with BioRender (www.biorender.com/). In (C)–(F), nuclei were counterstained with DAPI. In (B), three independent replicates (donors; 2, 3, 5) with six technical replicates (monolayers) were examined; in (C)–(F), three independent replicates (donors; 2, 3, 5) with technical triplicates (monolayers) were examined.

the apical compartment between cells [42]. We confirmed the basolateral localization of adherens junction-associated E-CAD and the apical localization of microvilli-associated Villin (figure 1(F)), and the (sub)apical localization of F-actin (figure S4). Another sign of cell polarization was a clear localization of nuclei along basal membranes (figure 1(F)). Thus, monolayers exhibited inside-outside polarization, *i.e.* the apical side towards outside and the basal side towards inside the tube (lumen). Together, laminin 332 mediated expansion, hepatocyte-like differentiation and polarization of organoid cell monolayers on HFMs.

# 3.2. Hepatocyte-like HFM-grown monolayers display a higher gene expression of mature hepatocyte-specific albumin, and drug-metabolizing enzymes and transporters, as compared to standard organoid cultures

We compared the total transcriptome of HFMexpanded monolayers and HFM-expanded monolayers differentiated for 7, 14 and 21 d to both expanded and differentiated standard Matrigel dropletbased organoid cultures, and to the whole liver, all from matched or partly matched donors. A principal component analysis revealed that monolayer and organoid transcriptomes are substantially separated (about 8.5 units) from the liver sample cluster along the first principal component (PC1) that describes the most variation in data (figure 2(A)). Based on the second principal component (PC2) that illustrates the second largest variation of transcriptomes, we identified clear clusters of expanded and differentiated monolayers and organoids. mRNA profiles of differentiated organoids and expanded monolayers were similar and separated from differentiated monolayers by up to three units. The most distant cluster from differentiated monolayers were expanded organoids. We did not detect distinct clusters for the three different time points of differentiated monolayers, indicating gene expression stability over time. To further depict transcriptomic differences between differentiated monolayers and organoids, we conducted a functional annotation analysis using the bioinformatic tool DAVID. Genes upregulated in monolayers over organoids encode proteins that are involved in numerous biological processes active in mature hepatocytes, including retinol metabolism, drug/xenobiotic metabolism, lipid transport and metabolism, albumin secretion, aldehyde dehydrogenase activity and gluconeogenesis (figure 2(B)).

In particular, the expression of the classical lineage marker for mature hepatocytes *ALB* was significantly upregulated in differentiated monolayers versus differentiated organoids for all matched donors and was similar to the liver for one donor (figure S5(A)). We validated this pattern using

real-time qPCR (figure S2(B)). In line with the high level of mRNA for ALB, monolayers displayed a ubiquitous nuclear presence of the transcriptional master regulator for the hepatocyte lineage HNF4 $\alpha$  that governs ALB expression (figure S5(B)). Next, we focused on the expression of individual genes encoding proteins that participate in metabolism and transport of drugs. First, we examined the abundance of transcripts of phase I drugmetabolizing enzymes, both of the CYP450 (oxidases) [43] and non-CYP450 (oxidases, reductases, hydrolases) [44] family (figure 2(C)). The first cluster encompassed enzymes that were downregulated in differentiated monolayers (7, 14 and 21 d) versus the liver, CYP2D6, CYP1A2, CYP2B6 and CES1, for instance. The second cluster included enzymes that were partly expressed in differentiated monolayers at similar levels to the liver such as CYP3A4, CYP2C9, ADH4 and PON1. Of note, CYP3A4, the most important phase I CYP450 enzyme for drug metabolism [43], was upregulated in differentiated monolayers over differentiated organoids. The last cluster encompassed non-CYP450 enzymes that were upregulated in monolayers and/or organoids (both expanded and differentiated) over the liver, including FMO5, ABHD10, CBR1 and ALDH1A1. Furthermore, we analyzed gene expression of phase II drug-metabolizing enzymes that drive conjugation reactions, i.e. UGTs (glucuronidation) [45], SULTs (sulfation) [46], NAT2 (acetylation) [44] and GSTs (glutathione conjugation) [47] (figure 2(D)), which was similar to the liver in differentiated monolayers of some donors. In addition, UGT1A1, UGT1A6, SULT1A1 and NAT2 were upregulated in differentiated monolayers over differentiated organoids. Based on the average expression of CYP3A4 and UGT1A6, differentiated monolayers significantly outperformed differentiated organoids and were comparable to the liver (figure S6). We validated this pattern for CYP3A4 using real-time qPCR (figure S2(B)). Finally, gene expression analysis of drug transporters [42] revealed a cluster that was upregulated in monolayers and organoids (both expanded and differentiated) over the liver, including basolateral uptake transporters such as SLCO1B3 (OATP1B3, anionic drugs) and SLC22A3 (OCT3, cationic drugs), basolateral efflux transporters, ABCC3 (MRP3) and ABCC4 (MRP4), and apical efflux transporters, ABCG2 (BCRP) and ABCB1 (MDR1) (figure 2(E)). The expression of SLCO2B1 (OATP2B1, basolateral uptake of anionic drugs) in differentiated monolayers was similar to the liver. SLC10A1 (NTCP, basolateral uptake), ABCC2 (MRP2, apical efflux) and ABCB4 (MDR3, apical efflux) were expressed in some differentiated monolayers at the levels observed in the liver. Other transporters such as SLCO1B3 (OATP1B1, basolateral uptake of anionic drugs), SLC22A1 (OCT1,

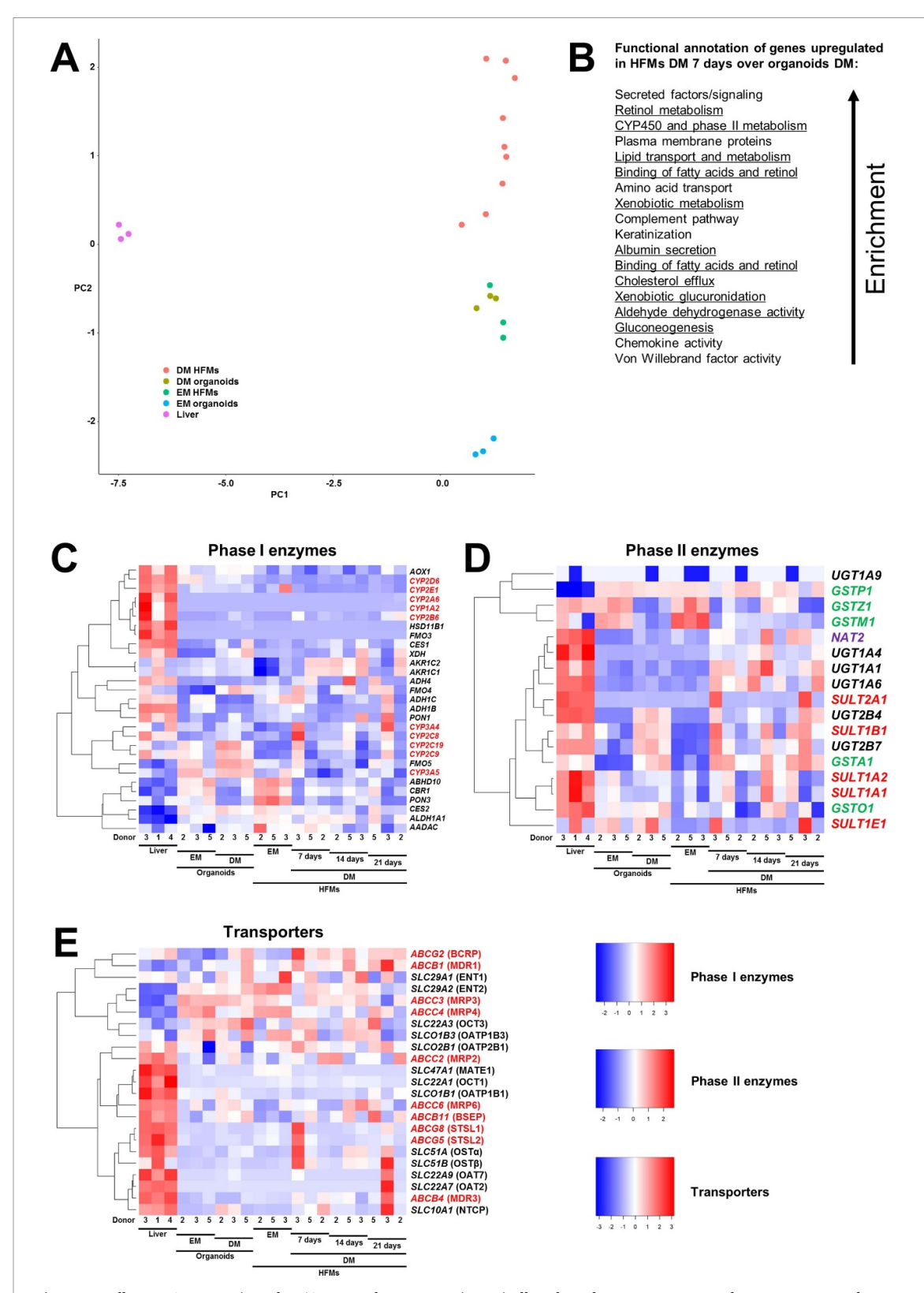


**Figure 2.** Bulk mRNA sequencing of PK/ADME-relevant genes in statically cultured HFM-grown monolayers, as compared to organoids and liver tissue. (A) A principal component analysis. (B) A functional annotation of genes upregulated in differentiated monolayers (7 d) over differentiated organoids. (C) A heatmap for gene expression of phase I drug-metabolizing enzymes. (D) A heatmap for gene expression of phase II drug-metabolizing enzymes. (E) A heatmap for gene expression of drug transporters. Data information: in (B), biological processes specific to mature hepatocytes are underlined. In (C), CYP450 and non-CYP450 enzymes are marked in red and black, respectively. In (D) and (E), different enzyme or transporter families are marked with different colors. In (C)–(E), the heatmaps show normalized log2 gene expression. A 5% FDR (adjusted P-value <0.05) cut-off was applied. Values were scaled (z-score by row) with breaks from  $\leq$  –2 to  $\geq$ 3 in C,  $\leq$  –2 to  $\geq$ 2 in D and  $\leq$  –3 to  $\geq$ 3 in (E). In (A)–(E), three independent replicates (donors, marked) per condition were examined. Matched donors (2, 3, 5) were used for organoids and monolayers. In (A) and (C)–(E), donor 3 matched liver tissue, organoids and monolayers, and two other donors (1, 4) were used for liver tissue.

basolateral uptake of cationic drugs) and *SLC47A1* (MATE1, apical efflux) were downregulated in differentiated monolayers versus the liver. In line with the principal component analysis, long-term differentiation of monolayers did not clearly alter gene expression of drug-metabolizing enzymes and transporters. Together, gene expression in differentiated monolayers was more comparable to liver tissue than to differentiated organoids.

## 3.3. Hepatocyte-like HFM-grown monolayers exhibit functional transport and metabolism of drugs

We observed a ubiquitous or an abundant membranous presence of representative transporters for basal uptake (OATP1B3 and OCT1) or efflux (MRP3) and for apical efflux (MDR1, MRP2 and BCRP) in differentiated HFM-grown monolayers (figure 3(A)). In addition, the apical localization of nearly ubiquitously expressed MDR1 (efflux) and the basolateral localization of ubiquitously expressed NTCP (uptake) was confirmed (figures 3(B) and (C)), in line with the previous data on monolayer polarization (figure 1(F)). It was possible to detect a high protein expression of OCT1, despite lower transcript levels, as compared to the liver. For the functional examination of selected transporters, we used calcein-AM that enters cells via passive diffusion and is effluxed by MDR1 or is first hydrolized intracellularly into the fluorescent anion calcein that is effluxed by BCRP and MRPs [48, 49]. Blocking efflux of calcein-AM and calcein with a cocktail of reference inhibitors, i.e. PSC-833 (MDR1), KO143 (BCRP) and MK-571 (MRPs), resulted in a 5.3-fold increase in intracellular fluorescence of calcein (figures 3(D) and (E)), confirming that the efflux transporters were active.

To study the oxidative capacity of phase I drugmetabolizing enzymes in differentiated HFM-grown monolayers, we examined a cocktail of FDA US reference parent drugs [50] (figure 4(A)). Together, these enzymes mediate approximately 80% of CYP450associated metabolism of the top 200 most prescribed drugs (in the USA in 2014), with the most important CYP3A4 being responsible for 40% [43]. To examine phase II metabolism via glucuronidation by various UGTs, mainly UGT1A6 [51], 7-hydroxycoumarin (coumarin-OH) was used, which is the major phase I metabolite (via CYP2A6) of coumarin, a natural pharmaceutical [52]. Glucuronidation is the major phase II reaction, and UGTs jointly carry out 45% of non-CYP450-associated metabolism of the top 200 most prescribed drugs [43]. Metabolism-driven clearance of midazolam and coumarin in the liver, via the so-called first-pass effect, is rapid and extensive. Clearance of dextromethorphan and phenacetin is moderate. In turn, tolbutamide and bupropion are

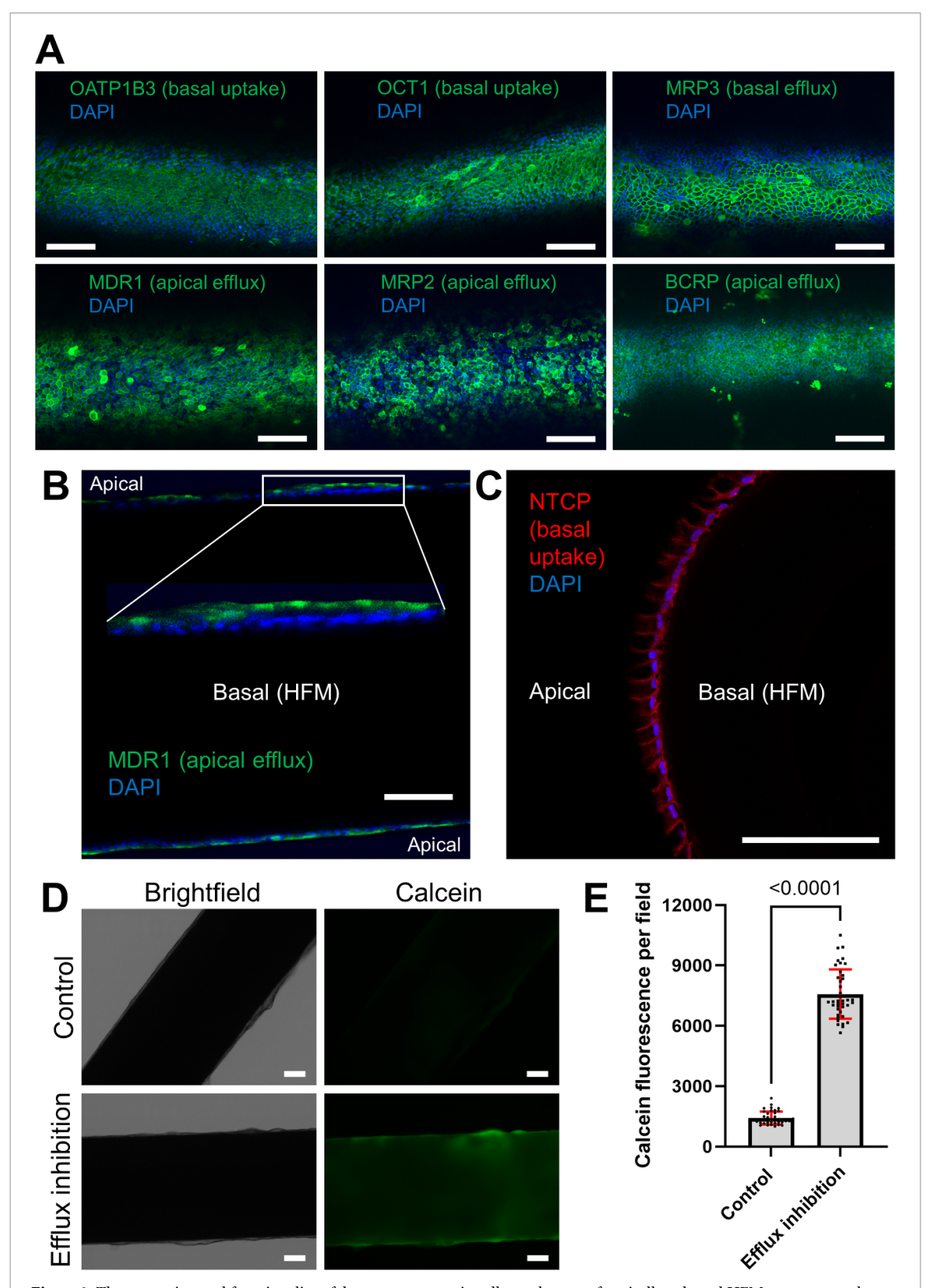
considered low-clearance drugs [52–54]. We compared the metabolizing performance of monolayers to standard organoid cultures from matched donors and PHH sandwich collagen I cultures (figure 4(B)). We detected metabolites for all the parent compounds in all monolayer cultures, in contrast to organoid cultures with a limited metabolizing capacity. The most extreme case was the lack of bupropion-OH formed in all organoid cultures. The production of midazolam-OH in monolayers was at a similar level to PHH cultures. However, PHHs outperformed monolayers in the formation of the remaining metabolites.

Next, we explored the biotransformation kinetics of midazolam over 24 h in donor 3 monolayers with the highest conversion and donor 5 monolayers with the lowest metabolizing capacity (figure 4(B)). The major primary metabolite of midazolam, 1'hydroxymidazolam (midazolam-OH), is further transformed into 1'-hydroxymidazolam glucuronide (midazolam-OH-GLU) by two other UGT enzymes, i.e. UGT2B4 and UGT2B7 [55]. Donor 3 monolayers showed a 7-fold higher capacity to form midazolam-OH and a 14-fold increase in the formation of midazolam-OH-GLU after 24 h, as compared to donor 5 monolayers (figure S7(A)). In addition, the production of both midazolam-OH and midazolam-OH-GLU in donor 5 monolayers reached saturation already after 16 h. These findings were reflected by an upregulated expression of CYP3A4, UGT2B4 and UGT2B7 in donor 3 over donor 5 monolayers (figures 2(C) and (D)).

The interaction between midazolam and keto-conazole is a classical example of a drug-drug interaction. Ketoconazole can compete for CYP3A4, compromising the conversion of midazolam to midazolam-OH [56]. Upon exposure to keto-conazole, we demonstrated a reduced formation of midazolam-OH and midazolam-OH-GLU in both donor 3 and 5 monolayers (figure S7(B)). Together, the hepatocyte-like HFM-based system allows for studying phase I and II metabolism of drugs in a personalized fashion by capturing donor-to-donor variations in the activity of biotransforming enzymes. Moreover, the system is suitable to examine active transport of drugs across cell membranes.

# 3.4. Hepatocyte-like HFM-grown monolayers display transport and metabolism of drugs on-a-chip

The ultimate step in advancing our model was coupling it to a micro-/millifluidic system using biocompatible in-house-3D printed chips. We grew and differentiated organoid fragments on HFMs immobilized on inserts that were then placed into biochambers. By this, two microfluidic compartments were



A Myszczyszyn et al

Figure 3. The expression and functionality of drug transporters in cell membranes of statically cultured HFM-grown monolayers that were differentiated for 7 d. (A) A representative whole-mount confocal immunofluorescence microscopy image of OATP1B3, OCT1, MRP3, MDR1, MRP2 and BCRP in a dorsal section of a HFM. (B) A representative whole-mount confocal immunofluorescence microscopy image for the apical localization of MDR1 in a median section of a HFM. (C) A representative confocal immunofluorescence microscopy image for the basolateral localization of NTCP in cell membranes of a monolayer in an anterior section of a HFM. (D) Representative brightfield images and images of intracellular fluorescence of calcein of monolayers treated with efflux inhibitors versus DMSO (control). (E) The quantification of calcein fluorescence. Data information: scale bars in (A)–(D), 100  $\mu$ m. In (A)–(C), nuclei were counterstained with DAPI. In (E), the graph shows mean  $\pm$  SD (error bars). In (A)–(C), three independent replicates (donors; 2, 3, 5) with technical triplicates (monolayers) were examined. In (D) and (E), one independent replicate (donor, 5) with 40 technical replicates (fields) from two monolayers (20 replicates each) was examined. In (E), data did not pass the Shapiro-Wilk normality test ( $\alpha$  = 0.05). Thus, the non-parametric Mann-Whitney U test was performed (P-value <0.05).

Enzyme(s)	Parental compound	Oxidative or conjugation reaction	Metabolite	Phase	% of the top 200 most prescribed drugs	
CYP3A4	Midazolam	Hydroxylation	Midazolam-OH		40	
CYP2D6	Dextromethorphan	O-demethylation	Dextrorphan		21	~80
CYP2C9	Tolbutamide	Methyl-hydroxylation	Tolbutamide-OH	(CYP450)	9	
CYP1A2	Phenacetin	O-deethylation	Acetaminophen		9	
CYP2B6	Bupropion	Hydroxylation	Bupropion-OH		<3	
UGTs (mainly UGT1A6)	Coumarin-OH	Glucuronidation (conjugation)	Coumarin-OH-GLU	II (non-CYP450)	45	

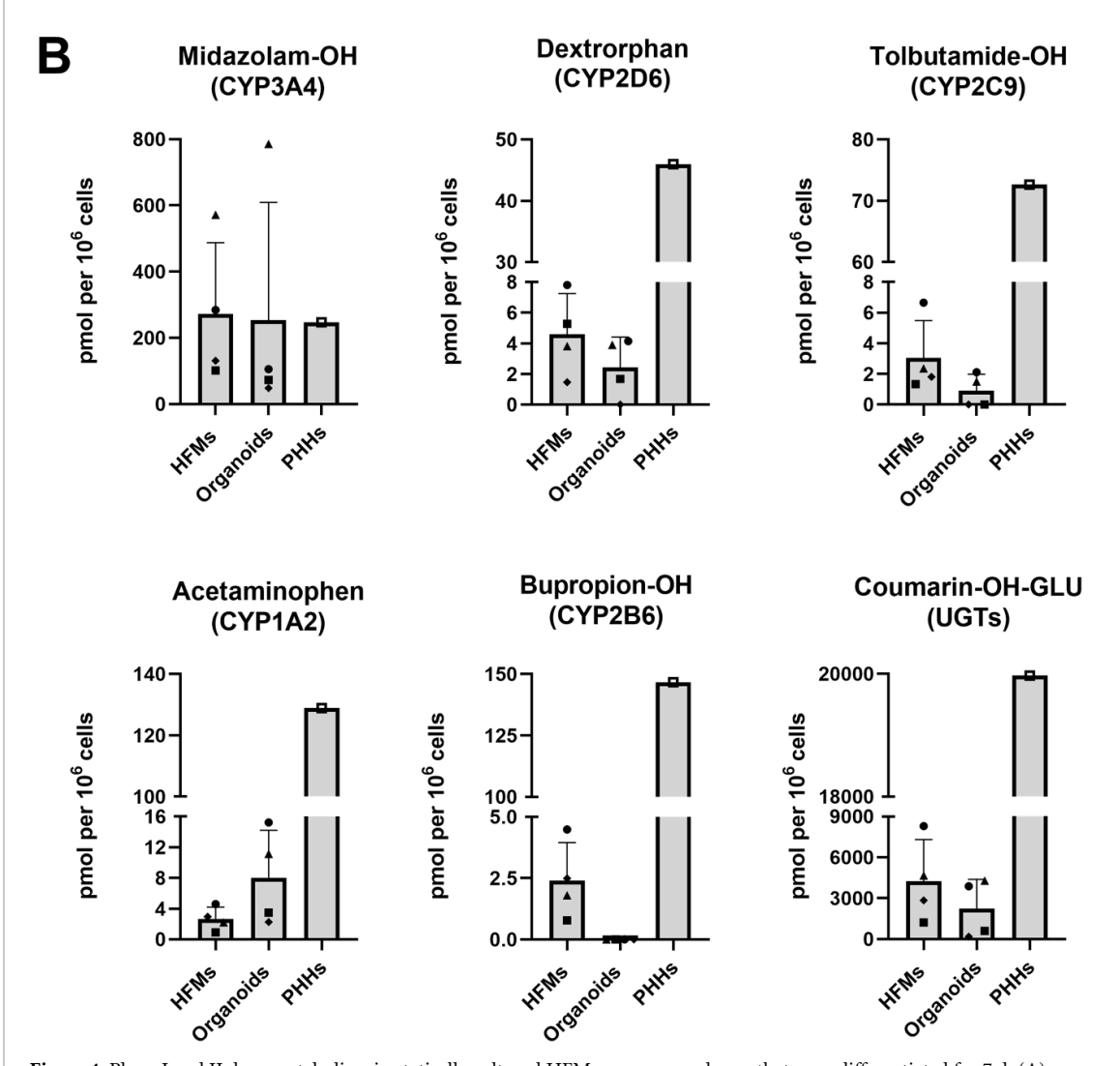


Figure 4. Phase I and II drug metabolism in statically cultured HFM-grown monolayers that were differentiated for 7 d. (A) Characteristics of selected parent compounds used for testing the activity of the most important phase I and II drug-metabolizing enzymes. (B) The formation of metabolites of the parent compounds in monolayers, as compared to organoids and collagen I sandwich PHHs. Data information: in (B), the graphs show mean + SD (error bars). Four independent matched replicates (donors; 1–3, 5) were examined for monolayers and organoids. For monolayers, one technical replicate (well/measurement, from pooled six monolayers); and for organoids, two averaged technical replicates (wells/measurements) were examined per donor. PHHs are from a pool of 10 independent replicates (donors, five males and five females) with technical triplicates (wells/measurements). Not all data passed the Shapiro-Wilk normality test ( $\alpha = 0.05$ ). Thus, the non-parametric Kruskal-Wallis test followed by the Dunn's multiple comparison test was performed (P-value < 0.05). All comparisons were non-significant due to high inter-donor variance (SD), values of 0 and pooled PHHs. However, trends were observed.

created, *i.e.* a perfusable basal/blood-like compartment inside HFMs and a static apical/canalicular-like compartment outside HFMs. We perfused the system with FITC-dextran (FD4) solution for 10 min with a speed of 50  $\mu$ l min<sup>-1</sup> (3 ml h<sup>-1</sup>) (figure 5(A)) that is within the standard range of 2–6 ml h<sup>-1</sup> applied for HFM-based systems previously [15, 18–20]. We confirmed the functional barrier integrity of monolayers of both donors, as demonstrated by 10 times lower paracellular passive diffusion of FD4 to the apical compartment, *i.e.* apparent permeability ( $P_{\rm app}$ ) [33], as compared to cell-free HFMs (coated with L-DOPA and laminin 332, a positive control) (figure 5(B)). Nail polish-coated HFMs served as a tight barrier (a negative control).

Next, the disposition of midazolam was studied on-a-chip. To minimize the so-called dead volume and thus to enable detection of the metabolites [11], we designed a circulation system with a 4 ml volume (figure 5(C)). Over three hrs, donor 3 monolayers metabolized 42% and donor 5 monolayers 37% of midazolam (figure S8(A)). Based on linear fragments of logarithmic depletion curves of midazolam (figure S8(B)), we determined slopes that were necessary to calculate its intrinsic clearance (CLint) [11, 39] (figure 5(D)). CLint for donor 3 monolayers was 1.3-fold higher, as compared to donor 5 monolayers. In line with the data generated on the statically cultured system, donor 3 monolayers produced higher amounts of midazolam-OH and midazolam-OH-GLU, as compared to donor 5 monolayers (figure 5(E)). For both donor monolayers, we observed an equilibrium of midazolam-OH between the basal and apical compartment. This is explained by the lack of active transporters specific for hydrophobic and highly permeable parental midazolam [57] and possibly for relatively hydrophobic and permeable midazolam-OH. In turn, we detected higher amounts of midazolam-OH-GLU in the basal compartment for both donor monolayers, which is the result of active transport likely via MRP3 (figure 3(A)) that pumps the hydrophilic metabolite to the circulation [58] for renal excretion [55]. Of note, a qualitative morphological evaluation of monolayers did not reveal any visible damage after 3 h perfusion (figure S9(A)). In line with this, barrier integrity was maintained over time, as shown by a quantitative detection of FD4 in the apical compartment after 10 min and three hrs of perfusion (figure S9(B)).

Finally, we established a proof-of-concept for a multi-organ-on-a-chip platform by perfusing the hepatocyte-like system for three hrs with a basal effluent from a statically cultured organoid-based small intestine-like Transwell system [40] to study the first-pass effect and bioavailability of midazolam and coumarin upon oral administration (apical/luminal-like

compartment) (figure 6(A)), similar to previous dual-organ system studies using different compounds [59–62]. The most efficient metabolizer was used, donor 3 monolayers. Midazolam-OH was produced by both small intestine- and hepatocyte-like monolayers (figure 6(B)), in line with CYP3A4 expression in the small intestine [63]. However, we did not detect midazolam-OH-GLU due to a low amount of midazolam that diffused to the basal effluent of the small intestine-like system, i.e. 3.4%. Ultimately, we found 2.3% of the midazolam dose in the basal compartment of the hepatocyte-like system (bioavailability). In contrast, coumarin was metabolized to coumarin-OH, followed by its glucuronidation, in the hepatocyte-like system only thanks to an exclusive activity of the minor phase I enzyme CYP2A6 [43, 50] (figure 6(C)). Detection of coumarin-OH was possible despite a lower expression of CYP2A6 in comparison to PHHs (figure 2(C)). The bioavailability of coumarin was 3.3%. Together, the hepatocytelike HFM-based system on-a-chip maintains a tight barrier over 3 h perfusion and allows for examining the disposition and bioavailability of high-clearance drugs, namely midazolam and coumarin.

### 4. Discussion

Despite the recent progress in developing human microphysiological systems, 3Rs-complied (animal component-free) liver-on-a-chip models that are suitable for examining both metabolism and transepithelial transport of drugs remain an unmet need for preclinical PK/ADME testing. Here, we filled this gap with a pioneering millifluidic hepatocyte-like system based on organoid-derived polarized monolayers grown on HFMs coated with recombinant human laminin 332. Hence, our model allows for studying uptake of parent compounds from the perfusable basal/blood-like compartment, and excretion of those compounds and their metabolites to the static apical/canalicular-like compartment or back to the circulation. In addition, the system displays improved hepatocyte-like maturation and functionality over standard organoid cultures from matched donors, similar to our previous bile duct-on-a-chip HFM-based model [20]. We believe that this is the result of a concerted action of the 3D HFM scaffold, laminin 332, organoid cells and growth factors in differentiation medium. Chip systems utilizing human organoid-derived cells are considered the most powerful in vitro models for preclinical drug development in the future [64], once standardized [65].

The HFMs in our study are commercially available and we successfully utilized them before for establishing multiple organ-on-a-chip systems that mimicked perfusion between blood and epithelial

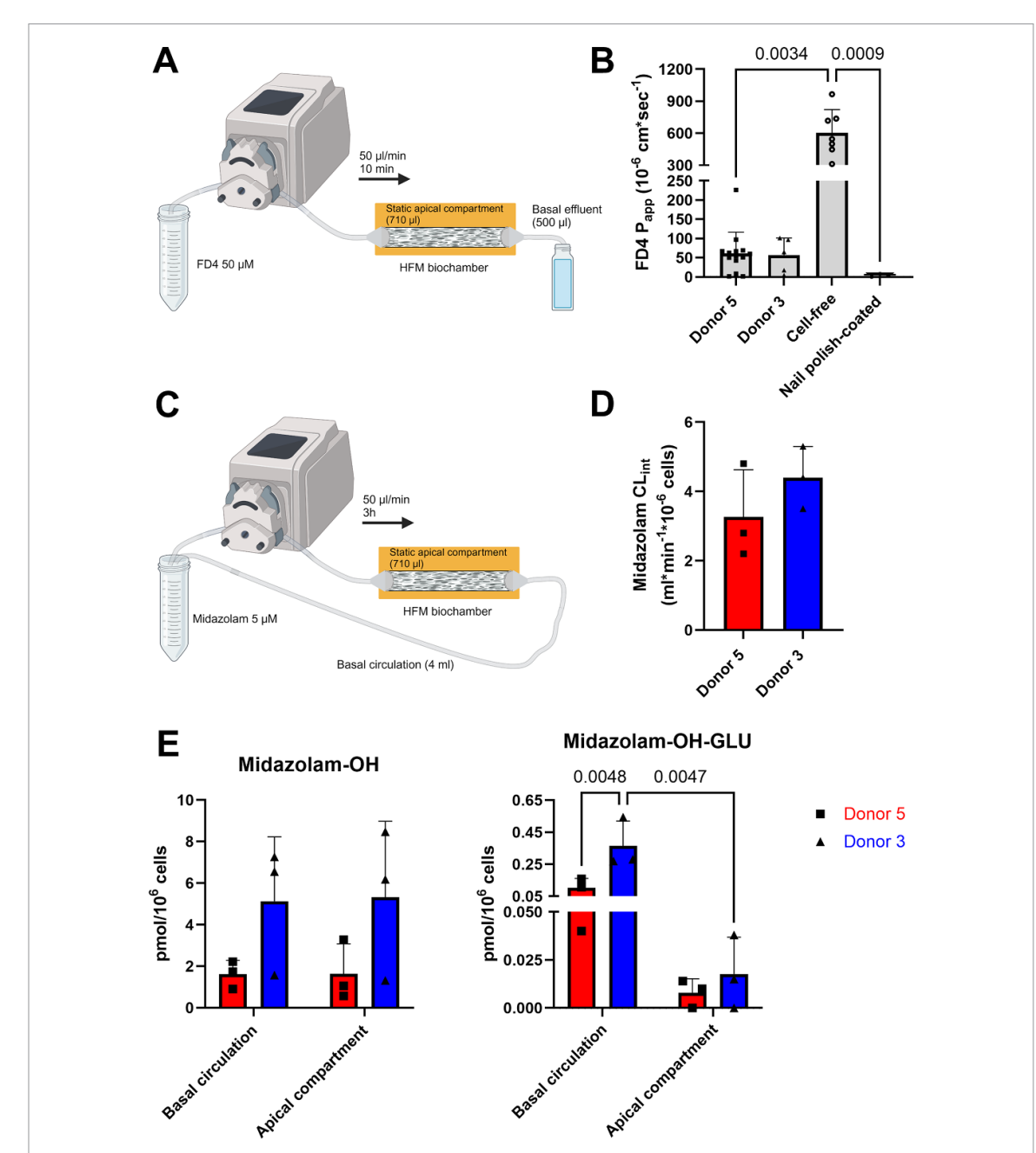
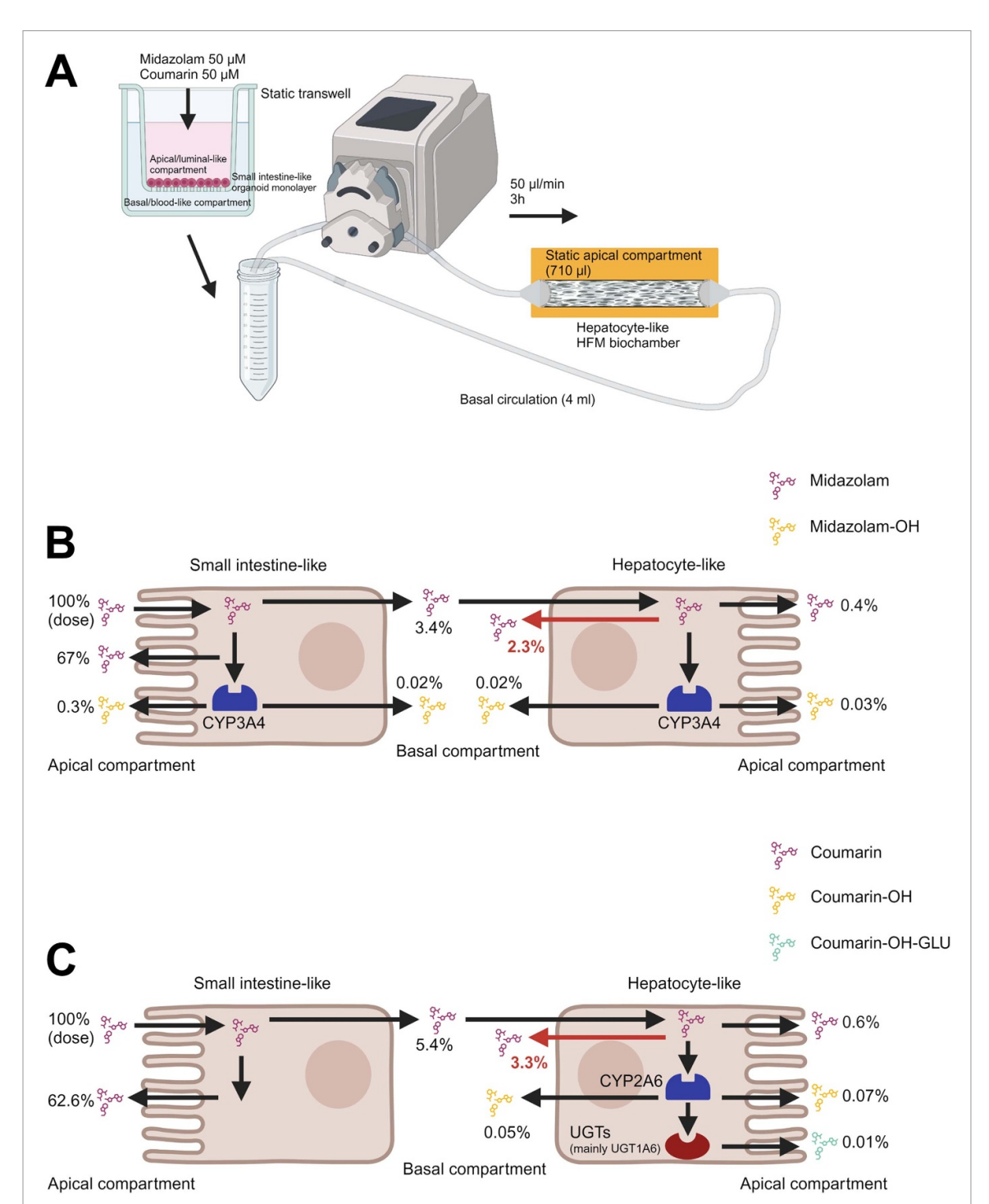


Figure 5. The functional barrier integrity of HFM-grown and differentiated (7 d) monolayers and the disposition of midazolam on-a-chip. (A) A scheme for the 10 min perfusion setup. (B) FD4  $P_{\rm app}$  of monolayers, as compared to cell-free HFMs (a positive control) and nail polish-coated HFMs (a negative control) after 10 min perfusion. (C). A scheme for the 3 h perfusion setup. (D) CLint of midazolam in monolayers over 3 h perfusion. (E) The disposition of midazolam-OH and midazolam-OH-GLU in the basal circulation and static apical compartment after 3 h perfusion. Data information: in (A) and (C), the schemes were created with BioRender (www.biorender.com/). In (B), (D) and (E), the graphs show mean + SD (error bars). In (E), midazolam-OH  $concentrations \ were \geqslant LOQ \ and \ midazolam-OH-GLU \ concentrations \ were \leqslant LOQ \ and \ \geqslant LOD. \ In \ (A) \ and \ (B), \ two \ independent \ (A) \ and \ (B) \ (B)$ replicates (donors; 3, 5) with five and 14 technical replicates (chips) were examined, respectively. Seven and three independent replicates of cell-free and nail polish-coated HFMs were analyzed, respectively. In (C)–(E), two independent replicates (donors; 3, 5) with technical triplicates (chips) were examined. In (B), not all data passed the Shapiro-Wilk normality test ( $\alpha = 0.05$ ). Thus, the non-parametric Kruskal-Wallis test followed by the Dunn's multiple comparison test was performed (P-value <0.05). The comparison donor 3 versus cell-free was non-significant, despite a strong trend observed for high numbers of technical replicates. In (D), data passed the Shapiro-Wilk normality test ( $\alpha = 0.05$ ). Thus, the t test with the Welch's correction (different SDs) was performed (P-value < 0.05). To make an observed trend significant, the number of technical replicates should probably be increased. In (E), the Shapiro-Wilk normality test ( $\alpha=0.05$ ) was not applicable. The two-way ANOVA test followed by the uncorrected Fisher's LSD multiple comparison test was performed (P-value < 0.05). Despite strong trends observed for some comparisons, they were non-significant. Increasing the number of technical replicates could overcome this limitation.



**Figure 6.** Connecting the liver-on-a-chip system to a statically cultured small intestine-like Transwell system. (A) A scheme for the connection to the statically cultured small intestine-like Transwell system. (B) The disposition of midazolam and midazolam-OH in the apical compartment and basal effluent of the small intestine-like system, and in the basal circulation and static apical compartment of the hepatocyte-like system after the administration of 50  $\mu$ M midazolam over two hrs, followed by 3 h perfusion. (C) The disposition of coumarin, coumarin-OH and coumarin-OH-GLU in the apical compartment and basal effluent of the small intestine-like system, and in the basal circulation and static apical compartment of the hepatocyte-like system after the administration of 50  $\mu$ M coumarin over two hrs, followed by 3 h perfusion. Data information: In (A)–(C), the schemes were created with BioRender (www.biorender.com/). One independent replicate (donor, 3) with technical triplicates (chips) was examined.

cells [15, 18-20]. However, the technical parameters of HFMs should be improved to recapitulate the microarchitecture of the liver. The length and diameter of the sinusoid is 275  $\mu$ m and 10  $\mu$ m, respectively [66]. In turn, HFMs are 300  $\mu$ m in diameter and we measured that the HFM length accounting for drug transport within the chip is 23 800  $\mu$ m. The ratio length to diameter is 27.5 to 1 for the sinusoid and 79 to 1 for HFMs. To recapitulate the ratio for the sinusoid, an upscaled length of HFMs within the chip should be shortened to 8250  $\mu$ m, that is by 2.9 times. In this scenario, also a difference in the thickness of the sinusoidal endothelial cell monolayer and HFM wall may be important, which is 11  $\mu$ m [66] and 100  $\mu$ m, respectively (1 to 9 ratio). Moreover, an upscaled cell number has to be considered. The sinusoid is surrounded by five hepatocytes, on average [67]. The surface area of the sinusoid and HFMs (with the shortened length) is  $27\,632 \ \mu\text{m}^2$  and  $12\,952\,500 \ \mu\text{m}^2$ ; respectively (with the ratio 1 to 469, including the thickness of the endothelial monolayer/HFM wall). This means that shortened HFM-grown monolayers should consist of 2344 cells, which contradicts the actual (counted) cell number by a factor of 100. Nevertheless, the higher actual cell number ensures reproducibly sensitive measurements in functional metabolic assays. Another important parameter for drug permeability between blood and the perisinusoidal space is fenestration of the endothelial monolayer with pore sizes ranging 100-1000 nm [66]. HFM pores are 500 nm in diameter that is in the middle of this range.

We identified laminin 332 as the most efficient driver of expansion of organoid fragments on HFMs, resulting in full coverage, as well as of hepatocyte-like differentiation. Enhancing the proliferative capacity is in line with studies in mice with acute liver injury that showed a dense deposition of laminins critical for hepatocyte progenitor cell-mediated regeneration [24, 68]. In agreement with it, adult stem cell-derived organoids are believed to recapitulate epithelial regenerative processes during their expansion phase [69]. Though, laminin 332 seems the least obvious choice from all commercially available recombinant human laminins for increasing hepatocyte-like maturation, as only one study linked it with the adult liver during homeostatic maintenance [23]. Furthermore, this laminin can support cholangiocyte-like differentiation in vitro [70].

By using organoids derived from four donors of both sexes, we were able to capture inter-individual variabilities in the expression and activity of drugmetabolizing enzymes and drug transporters. To ensure a personalized approach, generating data from more donors of both sexes and various ages is necessary. An added value will be the knowledge on clinically-relevant genetic polymorphisms of drugmetabolizing enzymes [71] and drug transporters [42] of those individuals. Our liver-on-a-chip system allowed for determining experimental kinetic parameters of drugs and their metabolites upon at least 3 h perfusion, which is a progress in comparison to our previous HFM-based systems with perfusion applied for only 10–13 min [15, 18–20]. We examined the basal and apical disposition of midazolam that is the substrate for the most important drug-metabolizing enzyme CYP3A4, whose role will even increase in a long-term perspective by driving metabolism of 64% of all newly approved drugs [43]. Examining phase II metabolism-related conjugation reactions other than the most frequently detected glucuronidation such as sulfation and acetylation [54], will also be an important element for further development of the model.

Despite our advancements, metabolizing capacity of the statically cultured system was lower for five out of the six compounds tested, as compared to PHHs, with only the formation of midazolam-OH being at the similar level. However, the liver-on-a-chip system exhibited three to six times reduced clearance of midazolam, as compared to PHHs in two existing millifluidic systems [11, 39]. To overcome these limitations, cell functionality may be improved by modifying the cocktail of growth additives, transcription factor engineering and incorporating additional ECM components relevant for the microenvironment of mature hepatocytes [72-74]. In particular, mesenchymal stem cell (MSC)-conditioned medium could be utilized to more closely mimic complex paracrine signaling [75], and MSC-decellularized HFMs could serve as a source of numerous ECM components that cannot be recreated exogenously [76]. Low oxygen treatment is also worth considering, as drugmetabolizing enzymes are expressed in the hypoxic pericentral zone of the liver [77]. Moreover, longer perfusion (up to 96-120 h) should be applied to enable detection of the metabolites of low-clearance drugs [11, 39]. A further added value of longer perfusion may be a flow-induced shear stress, another determinant of cell maturation [78]. Inducing shear stress also during the cell differentiation phase may be a synergistic option to enhance the expression of drug-metabolizing enzymes. Previously, we found that this stressor improved maturation of Caco-2 cells grown on HFMs [15].

To evaluate preclinical predictiveness of our system for PK/ADME, *in vitro* data have to be mechanistically and quantitatively extrapolated into human profiles using *in silico* physiologically-based pharmacokinetic (PBPK) mathematical modeling [11, 39, 79]. In particular, the digital twins (DigiLoCS) tool was recently demonstrated to outperform standard

tools by accounting for advanced biology, fluidic dynamics and chip architecture [80]. DigiLoCS significantly improved predictiveness of current liveron-a-chip models that underpredicted intrinsic clearance of drugs, including two existing millifluidic systems [11, 39]. Clearance of midazolam was now predicted with 100% accuracy. In addition, IVIVE for low-clearance drugs such as tolbutamide was increased. Our system also seems underpredictive, at least based on *in vitro* clearance values. Thus, PBPK modeling should be a follow-up of our study.

We demonstrated that hepatocyte-like monolayers formed the barrier that was 10 times tighter than porous HFM walls coated with L-DOPA and laminin 332. Monolayers generated in previous studies displayed higher permeability, with only a 3-4 fold change between cell-free and cell-laden HFMs [15, 18–20]. Ideally, permeability of differentiated Caco-2 monolayers should be examined using our system, which are known to form a tight barrier [15]. This will allow for determining a maximum acceptable cut-off value for permeability of hepatocyte-like monolayers. As we observed a variation in the functional barrier integrity of monolayers that we judged as confluent, establishing quantitative control criteria in addition to microscopic visualization prior to perfusion assays could reduce this variation.

Upon connecting our model to a statically cultured organoid-based small intestine-like Transwell system, we were able to study the bioavailability of high-clearance drugs. An in-house printed Transwell system that we previously used to establish tissue explant- and organoid-based small intestine-on-achip models [33, 81] as well as our HFM-based kidney proximal tubule-like microfluidic model [18] may be compatible to our system. An ultimate goal in the future should be connecting these three PK/ADMErelevant models in a physiologically accurate fashion into a multi-organ-on-a-chip platform for a full prediction of human profiles [7]. We believe that our liver-on-a-chip system can also be used for pharmacological applications other than predicting PK/ADME. In particular, the system can be maintained in differentiation medium in a broad functional time window that is suitable for examining acute hepatotoxicity of drug candidates with both an immediate and a delayed onset [82], and for examining a repeated dosing [83]. Indeed, a performance assessment of 870 commercially manufactured (from Emulate, Inc.) human liver-like chips confirmed that they are predictive for acute druginduced liver injury and can be incorporated into preclinical development for hepatotoxicity testing [84]. Finally, HFMs can be utilized in accordance with our protocol for creating organoid-derived perfusable

monolayers from other epithelial organs, for instance, breast [85], to study transepithelial transport across the highly selective blood-milk barrier to predict exposure to medication via breastfeeding [86]. In conclusion, we provide a proof-of-concept, bioengineered and animal component-free liver organoid-on-a-chip model for examining both metabolism and transport of drugs.

### Data availability statement

The data that support the findings of this study are openly available at the following URL/DOI: www.ncbi.nlm.nih.gov/geo/query/acc.cgi?acc=GSE269150/.

### Acknowledgments

We would like to thank our consortium partners for their valuable contribution, i.e. Birk Poller, Markus Walles, Olivier Kretz and Katharina Root from Novartis; Martijn Wilmer, Ron Byron, Errol Byron and Susan Veissi from Cell4Pharma; Joanne Donkers from TNO; Saskia Aan and Anne Burgers from Proefdiervrij as well as Margot Beukers from the Association of Collaborating Health Foundations (SGF). Moreover, we acknowledge the Utrecht Sequencing Facility (USEQ) for providing sequencing service and data. USEQ is subsidized by the University Medical Center Utrecht and The Netherlands X-omics Initiative (NWO Project 184.034.019). Furthermore, we thank Louis C Penning from the Faculty of Veterinary Medicine at the Utrecht University for his valuable comments on the revised version of the manuscript.

### **Funding**

This study is a part of a collaboration project that was co-funded by the PPP Allowance made available by Health~Holland, Top Sector Life Sciences & Health, to the Association of Collaborating Health Foundations (SGF) to stimulate public-private partnerships (LSHM20045-SGF).

### **Ethics statement**

The Medical Ethics Review Committee at the Erasmus Medical Center Rotterdam (EMC, The Netherlands) approved the research (MEC-2014-060). The research was conducted in accordance with the principles embodied in the Declaration of Helsinki and in accordance with local statutory requirements. All participants gave written informed consent to participate in the study. Consent was given for publication by all participants.

### **ORCID** iDs

Adam Myszczyszyn https://orcid.org/0009-0006-6152-5451

Anna Muench https://orcid.org/0009-0008-9560-3985

Vivian Lehmann https://orcid.org/0000-0002-5555-0486

Frank G van Steenbeek https://orcid.org/0000-0001-5460-6540

Manon Bouwmeester https://orcid.org/0000-0002-7141-9939

Marit Keuper-Navis https://orcid.org/0000-0001-8371-5594

Thomas K van der Made https://orcid.org/0000-0001-8714-3669

Luc J W van der Laan https://orcid.org/0000-0002-0651-5334

Hossein Eslami Amirabadi https://orcid.org/0000-0001-7940-5833

Rosalinde Masereeuw https://orcid.org/0000-0002-1560-1074

Bart Spee https://orcid.org/0000-0002-8114-0560

### References

- Waring M J et al 2015 An analysis of the attrition of drug candidates from four major pharmaceutical companies Nat. Rev. 14 475–86
- [2] Van Norman G A 2019 Limitations of animal studies for predicting toxicity in clinical trials: is it time to rethink our current approach? JACC 4 845
- [3] Stresser D M et al 2023 Towards in vitro models for reducing or replacing the use of animals in drug testing Nat. Biomed. Eng. 8 930–5
- [4] Musther H, Olivares-Morales A, Hatley O J D, Liu B and Rostami Hodjegan A 2014 Animal versus human oral drug bioavailability: do they correlate? Eur. J. Pharm. Sci. 57 280
- [5] Fowler S, Chen W L K, Duignan D B, Gupta A, Hariparsad N, Kenny J R, Lai W G, Liras J, Phillips J A and Gan J 2020 Microphysiological systems for ADME-related applications: current status and recommendations for system development and characterization Lab Chip 20 446–67
- [6] Ingber D E 2022 Human organs-on-chips for disease modelling, drug development and personalized medicine *Nat. Rev. Genet.* 23 467–91
- [7] Keuper-Navis M et al 2023 The application of organ-on-chip models for the prediction of human pharmacokinetic profiles during drug development *Pharmacol. Res.* 195 106853
- [8] Cox B, Barton P, Class R, Coxhead H, Delatour C, Gillent E, Henshall J, Isin E M, King L and Valentin J-P 2022 Setup of human liver-chips integrating 3D models, microwells and a standardized microfluidic platform as proof-of-concept study to support drug evaluation *Biomater. Biosyst.* 7 100054
- [9] Jang K J 2019 Reproducing human and cross-species drug toxicities using a Liver-Chip Sci. Transl. Med. 11 eaax5516
- [10] Mehta V, Karnam G and Madgula V 2024 Liver-on-chips for drug discovery and development Mater. Today Bio 27 101143
- [11] Rajan S A P *et al* 2023 A novel milli-fluidic liver tissue chip with continuous recirculation for predictive pharmacokinetics applications *AAPS J.* **25** 1–14
- [12] Rubiano A et al 2021 Characterizing the reproducibility in using a liver microphysiological system for assaying drug toxicity, metabolism, and accumulation Clin. Transl. Sci. 14 1049

- [13] Sugano K et al 2010 Coexistence of passive and carrier-mediated processes in drug transport Nat. Rev. 9 597–614
- [14] Dao Thi V L et al 2020 Stem cell-derived polarized hepatocytes Nat. Commun. 11 1677
- [15] Jochems P G M, van Bergenhenegouwen J, van Genderen A M, Eis S T, Wilod Versprille L J F, Wichers H J, Jeurink P V, Garssen J and Masereeuw R 2019 Development and validation of bioengineered intestinal tubules for translational research aimed at safety and efficacy testing of drugs and nutrients *Toxicol. In Vitro* 60 1–11
- [16] Deng X, Zhang G, Shen C, Yin J and Meng Q 2013 Hollow fiber culture accelerates differentiation of Caco-2 cells Appl. Microbiol. Biotechnol. 97 6943–55
- [17] Clause K C, Liu L J and Tobita K 2010 Directed stem cell differentiation: the role of physical forces Cell Commun. Adhes. 17 48
- [18] Jansen J *et al* 2015 Human proximal tubule epithelial cells cultured on hollow fibers: living membranes that actively transport organic cations *Sci. Rep.* 5 1–12
- [19] Chen C et al 2018 Bioengineered bile ducts recapitulate key cholangiocyte functions  $\it Biofabrication~10~034103$
- [20] Wang Z, Faria J, van der Laan L J W, Penning L C, Masereeuw R and Spee B 2022 Human cholangiocytes form a polarized and functional bile duct on hollow fiber membranes Front. Bioeng. Biotechnol. 10 868857
- [21] Marsee A et al 2021 Building consensus on definition and nomenclature of hepatic, pancreatic, and biliary organoids Cell Stem Cell 28 816–32
- [22] Huch M et al 2015 Long-term culture of genome-stable bipotent stem cells from adult human liver Cell 160 299
- [23] Watanabe M, Zemack H, Johansson H, Hagbard L, Jorns C, Li M, Ellis E and Liu X 2016 Maintenance of hepatic functions in primary human hepatocytes cultured on xeno-free and chemical defined human recombinant laminins PLoS One 11 e0161383
- [24] Kallis Y N, Robson A J, Fallowfield J A, Thomas H C, Alison M R, Wright N A, Goldin R D, Iredale J P and Forbes S J 2011 Remodelling of extracellular matrix is a requirement for the hepatic progenitor cell response *Gut* 60 525–33
- [25] Cameron K et al 2015 Recombinant laminins drive the differentiation and self-organization of hESC-derived hepatocytes Stem Cell Rep. 5 1250
- [26] Malta D F B, Reticker-Flynn N E, Da Silva C L, Cabral J M S, Fleming H E, Zaret K S, Bhatia S N and Underhill G H 2016 Extracellular matrix microarrays to study inductive signaling for endoderm specification Acta Biomater. 34 30–40
- [27] Kanninen L K et al 2016 Laminin-511 and laminin-521-based matrices for efficient hepatic specification of human pluripotent stem cells Biomaterials 103 86–100
- [28] Ong J et al 2018 Imaging-based screen identifies laminin 411 as a physiologically relevant niche factor with importance for i-Hep applications Stem Cell Rep. 10 693–702
- [29] Takayama K et al 2014 Prediction of interindividual differences in hepatic functions and drug sensitivity by using human iPS-derived hepatocytes Proc. Natl Acad. Sci. USA 111 16772–7
- [30] Wang Z, Ye S, van der Laan L J W, Schneeberger K, Masereeuw R and Spee B 2024 Chemically defined organoid culture system for cholangiocyte differentiation Adv. Healthcare Mater. 13 2401511
- [31] Ye S et al 2020 A chemically defined hydrogel for human liver organoid culture Adv. Funct. Mater. 30 2000893
- [32] Bouwmeester M C *et al* 2023 Drug metabolism of hepatocyte-like organoids and their applicability in *in vitro* toxicity testing *Molecules* 28 621
- [33] Eslami Amirabadi H et al 2022 Intestinal explant barrier chip: long-term intestinal absorption screening in a novel microphysiological system using tissue explants Lab Chip 22 326–42

- [34] Myszczyszyn A et al 2024 A hollow fiber membrane-based liver organoid-on-a-chip model for examining drug metabolism and transport Gene expression omnibus (GEO) (available at: https://www.ncbi.nlm.nih.gov/geo/query/acc. cgi?acc=GSE269150/)
- [35] Zhang Y, Parmigiani G and Johnson W E 2020 ComBat-seq: batch effect adjustment for RNA-seq count data NAR Genom. Bioinform. 2 lqaa078
- [36] Robinson M D and Oshlack A 2010 A scaling normalization method for differential expression analysis of RNA-seq data Genome Biol. 11 1–9
- [37] Robinson M D, McCarthy D J and Smyth G K 2010 edgeR: a Bioconductor package for differential expression analysis of digital gene expression data *Bioinformatics* 26 139–40
- [38] Wickham H 2016 Ggplot2: Elegant Graphics for Data Analysis 2nd edn (Springer)
- [39] Docci L et al 2022 Exploration and application of a liver-on-a-chip device in combination with modelling and simulation for quantitative drug metabolism studies Lab Chip 22 1187–205
- [40] Streekstra E J et al 2024 Human enteroid monolayers as a potential alternative for Ussing chamber and Caco-2 monolayers to study passive permeability and drug efflux Eur. J. Pharm. Sci. 201 106877
- [41] Yurchenco P D and Kulczyk A W 2024 Polymerizing laminins in development, health, and disease J. Biol. Chem. 300 107429
- [42] Galetin A et al 2024 Membrane transporters in drug development and as determinants of precision medicine Nat. Rev. 23 255–80
- [43] Saravanakumar A, Sadighi A, Ryu R and Akhlaghi F 2019 Physicochemical properties, biotransformation, and transport pathways of established and newly approved medications: a systematic review of the top 200 most prescribed drugs vs. the FDA-approved drugs between 2005 and 2016 Clin. Pharmacokinet. 58 1281–94
- [44] Fukami T, Yokoi T and Nakajima M 2022 Non-P450 drug-metabolizing enzymes: contribution to drug disposition, toxicity, and development Annu. Rev. Pharmacol. Toxicol. 62 405–25
- [45] Rowland A, Miners J O and Mackenzie P I 2013 The UDP-glucuronosyltransferases: their role in drug metabolism and detoxification *Int. J. Biochem. Cell Biol.* 45 1121–32
- [46] Isvoran A, Peng Y, Ceauranu S, Schmidt L, Nicot A B and Miteva M A 2022 Pharmacogenetics of human sulfotransferases and impact of amino acid exchange on Phase II drug metabolism *Drug Discov. Today* 27 103349
- [47] Hayes J D, Flanagan J U and Jowsey I R 2005 Glutathione transferases Annu. Rev. Pharmacol. Toxicol. 45 51–88
- [48] Caetano-Pinto P, Nordell P, Nieskens T, Haughan K, Fenner K S and Stahl S H 2023 Amplifying the impact of kidney microphysiological systems: predicting renal clearance using mechanistic modelling based on reconstructed drug secretion ALTEX 40 408–24
- [49] van Genderen A M et al 2021 Topographic guidance in melt-electrowritten tubular scaffolds enhances engineered kidney tubule performance Front. Bioeng. Biotechnol. 8 617364
- [50] Spaggiari D, Geiser L, Daali Y and Rudaz S 2014 A cocktail approach for assessing the *in vitro* activity of human cytochrome P450s: an overview of current methodologies *J. Pharm. Biomed. Anal.* 101 221–37
- [51] Juvonen R O, Heikkinen A T, Kärkkäinen O, Jehangir R, Huuskonen J, Troberg J, Raunio H, Pentikäinen O T and Finel M 2020 *In vitro* glucuronidation of 7-hydroxycoumarin derivatives in intestine and liver microsomes of Beagle dogs *Eur. J. Pharm. Sci.* 141 105118
- [52] Hsieh C J, Sun M, Osborne G, Ricker K, Tsai F C, Li K, Tomar R, Phuong J, Schmitz R and Sandy M S 2019 Cancer hazard identification integrating human variability: the case of coumarin *Int. J. Toxicol.* 38 501–52

- [53] Donato M T, Hallifax D, Picazo L, Castell J V, Houston J B, Gomez-Lechón M J and Lahoz A 2010 Metabolite formation kinetics and intrinsic clearance of phenacetin, tolbutamide, alprazolam, and midazolam in adenoviral cytochrome P450-transfected HepG2 cells and comparison with hepatocytes and in vivo Drug Metab. Dispos. 38 1449–55
- [54] Kratochwil N A et al 2017 Metabolic profiling of human long-term liver models and hepatic clearance predictions from in vitro data using nonlinear mixed-effects modeling AAPS J. 19 534–50
- [55] Zhu B, Bush D, Doss G A, Vincent S, Franklin R B and Xu S 2008 Characterization of 1'-hydroxymidazolam glucuronidation in human liver microsomes *Drug Metab*. *Dispos.* 36 331–8
- [56] Greenblatt D J, Zhao Y, Venkatakrishnan K, Duan S X, Harmatz J S, Parent S J, Court M H and von Moltke L L 2011 Mechanism of cytochrome P450-3A inhibition by ketoconazole J. Pharm. Pharmacol. 63 214–21
- [57] Umehara K, Cantrill C, Wittwer M B, Di Lenarda E, Klammers F, Ekiciler A, Parrott N, Fowler S and Ullah M 2020 Application of the extended clearance classification system (ECCS) in drug discovery and development: selection of appropriate in vitro tools and clearance prediction Drug Metab. Dispos. 48 849–60
- [58] Järvinen E, Deng F, Kiander W, Sinokki A, Kidron H and Sjöstedt N 2022 The role of uptake and efflux transporters in the disposition of glucuronide and sulfate conjugates *Front*. *Pharmacol.* 12 802539
- [59] Bricks T, Hamon J, Fleury M J, Jellali R, Merlier F, Herpe Y E, Seyer A, Regimbeau J-M, Bois F and Leclerc E 2015 Investigation of omeprazole and phenacetin first-pass metabolism in humans using a microscale bioreactor and pharmacokinetic models *Biopharm. Drug Dispos.* 36 275–93
- [60] Milani N, Parrott N, Ortiz Franyuti D, Godoy P, Galetin A, Gertz M and Fowler S 2022 Application of a gut-liver-on-a-chip device and mechanistic modelling to the quantitative in vitro pharmacokinetic study of mycophenolate mofetil Lab Chip 22 2853–68
- [61] Prot J M, Maciel L, Bricks T, Merlier F, Cotton J, Paullier P, Bois F Y and Leclerc E 2014 First pass intestinal and liver metabolism of paracetamol in a microfluidic platform coupled with a mathematical modeling as a means of evaluating ADME processes in humans *Biotechnol. Bioeng.* 111 2027–40
- [62] Tsamandouras N, Chen W L K, Edington C D, Stokes C L, Griffith L G and Cirit M 2017 Integrated gut and liver microphysiological systems for quantitative in vitro pharmacokinetic studies AAPS J. 19 1499
- [63] Yamashita T et al 2021 Monolayer platform using human biopsy-derived duodenal organoids for pharmaceutical research Mol. Ther. Methods Clin. Dev. 22 263
- [64] Zhao Y et al 2024 Integrating organoids and organ-on-a-chip devices Nat. Rev. Bioeng. 2 588–608
- [65] Nahon D M et al 2024 Standardizing designed and emergent quantitative features in microphysiological systems Nat. Biomed. Eng. 8 941–62
- [66] Ehrlich A, Duche D, Ouedraogo G and Nahmias Y 2019 Challenges and opportunities in the design of liver-on-chip microdevices Annu. Rev. Biomed. Eng. 21 219–39
- [67] Wake K and Sato T 2015 "The Sinusoid" in the liver: lessons learned from the original definition by charles Sedgwick Minot (1900) Anatomical Rec. 298 2071–80
- [68] Lorenzini S et al 2010 Characterisation of a stereotypical cellular and extracellular adult liver progenitor cell niche in rodents and diseased human liver GUT 59 645–54
- [69] Schutgens F and Clevers H 2020 Human organoids: tools for understanding biology and treating diseases Annu. Rev. Pathol. Mech. Dis. 15 211–34
- [70] Yamada M, Okada H, Kikkawa Y, Miyajima A and Itoh T 2020 Miyajima A and Itoh T 2020 Tissue substructure-specific deposition of the β3-containing laminin-332 in the biliary epithelium of human and mouse livers Biochem. Biophys. Res. Commun. 524 465–71

- [71] Zhou Y and Lauschke V M 2022 The genetic landscape of major drug metabolizing cytochrome P450 genes—an updated analysis of population-scale sequencing data *Pharmacogenomics J.* 22 284–93
- [72] Chen C, Soto-Gutierrez A, Baptista P M and Spee B 2018 Biotechnology challenges to *in vitro* maturation of hepatic stem cells *Gastroenterology* 154 1258–72
- [73] Hendriks D, Artegiani B, Margaritis T, Zoutendijk I, Chuva de Sousa Lopes S and Clevers H 2024 Mapping of mitogen and metabolic sensitivity in organoids defines requirements for human hepatocyte growth Nat. Commun. 15 1–15
- [74] Wu H et al 2025 Multi-omics analysis reveals distinct gene regulatory mechanisms between primary and organoid-derived human hepatocytes DMM Dis. Models Mech. 18 dmm050883
- [75] Takebe T, Zhang R-R, Koike H, Kimura M, Yoshizawa E, Enomura M, Koike N, Sekine K and Taniguchi H 2014 Generation of a vascularized and functional human liver from an iPSC-derived organ bud transplant *Nat. Protocols* 9 396–409
- [76] Zhang X, Chen X, Hong H, Hu R, Liu J and Liu C 2022 Decellularized extracellular matrix scaffolds: recent trends and emerging strategies in tissue engineering *Bioact. Mater.* 10 15
- [77] Paris J and Henderson N C 2022 Liver zonation, revisited Hepatology 76 1219
- [78] Hofer M and Lutolf M P 2021 Engineering organoids Nat. Rev. Mater. 6 402–20

- [79] Kuepfer L, Niederalt C, Wendl T, Schlender J-F, Willmann S, Lippert J, Block M, Eissing T and Teutonico D 2016 Applied concepts in PBPK modeling: how to build a PBPK/PD model CPT Pharm. Syst. Pharmacol. 5 516
- [80] Aravindakshan M R, Mandal C, Pothen A, Schaller S and Maass C 2025 DigiLoCS: a leap forward in predictive organ-on-chip simulations PLoS One 20 1–20
- [81] Keuper-Navis M et al 2024 Intestinal cells-onchip for permeability studies Micromachines 15 1464
- [82] Bessone F et al 2021 Drug-induced liver injury: a management position paper from the Latin American association for study of the liver Ann. Hepatol. 24 100321
- [83] Maschmeyer I et al 2015 Chip-based human liver-intestine and liver-skin co-cultures—a first step toward systemic repeated dose substance testing in vitro Eur. J. Pharm. Biopharm. 95 77–87
- [84] Ewart L et al 2022 Performance assessment and economic analysis of a human Liver-Chip for predictive toxicology Commun. Med. 2 1–16
- [85] Sachs N et al 2018 A living biobank of breast cancer organoids captures disease heterogeneity Cell 172 373–386.e10
- [86] Nauwelaerts N et al 2021 A comprehensive review on non-clinical methods to study transfer of medication into breast milk—a contribution from the ConcePTION project Biomed. Pharmacother. 136 111038